RSC Advances

ROYAL SOCIETY OF CHEMISTRY

PAPER

View Article Online
View Journal | View Issue

Check for updates

Cite this: *RSC Adv.*, 2025, **15**, 37325

Solvent-modulated second harmonic generation in *N*-alkylated thiohydantoin derivatives: synthesis, characterization, and first-principle insights

Muhammad Arif Ali, *[a] Muhammad Zahid Qureshi,[b] Rahman Shah Zaib Saleem,[c] Mariusz Mojzych,[d] Ahsan Sharif[e] and Muhammad Arshad *[a]

This study explores the synthesis (five new thiohydantoin derivatives from MAS1 to MAS5, while an REF molecule was used as a standard for comparative DFT studies), spectroscopic characterization, and optoelectronic properties of six newly designed thiohydantoin derivatives using a combined experimental and computational approach. The molecular structures of all synthesized compounds were confirmed through FTIR and NMR spectroscopy, while DFT calculations at four functionals provided insights into vibrational modes, chemical shifts, and electronic behavior. Among the utilized functionals D3-B3LYP demonstrated the best agreement with experimental data, establishing its reliability for predicting electric field induced second harmonic generation (EFISHG) and electro-optical Pockel's effect (EOPE). Frontier molecular orbital (FMO) analysis revealed a reduced energy gap in nitro-substituted derivatives, particularly MAS3 (ΔE = 3.32 eV), which exhibited enhanced intramolecular charge transfer (ICT) and large hyperpolarizabilities, responsible for EFISHG applications. Molecular electrostatic potential (MEP) maps highlighted significant charge separation, while ELF and LOL analyses confirmed strong π-electron delocalization, further supporting their electro-optic potential. Notably, MAS3 displayed the highest first hyperpolarizability (β_{tot} = 3217 a.u.), surpassing the reference *p*-nitroaniline (*p*NA), indicating strong potential for second-harmonic generation (SHG) and EOPE-based devices. Dynamic hyperpolarizability studies at 1460 nm and 1907 nm revealed frequency-dependent behavior, with MAS3 showing exceptional $\gamma(-2\omega;\omega,\omega,0)$ values (124 212 a.u.), suggesting utility in EFISHG measurements and electro-optic modulation. Thermodynamic stability, light-harvesting efficiency (LHE), and radiative lifetime (τ_r = 8.8 ns for MAS3) further underscore the promise of these derivatives for optoelectronic applications. This work not only validates the solvent modulated EFISHG and EOPE capabilities of thiohydantoin-based systems but also provides a robust framework for designing advanced organic materials for photonics and telecommunications.

Received 20th August 2025
Accepted 26th September 2025

DOI: 10.1039/d5ra06169e

rsc.li/rsc-advances

1 Introduction

The interaction of light with matter has been a cornerstone of scientific exploration for centuries, driving innovations that shape modern technology.[1,2] Among the many phenomena arising from this interaction, electric field induced second harmonic generation (EFISHG) stands out as a powerful tool for probing the nonlinear optical (NLO) properties of materials. Unlike conventional techniques that require crystalline alignment or complex setups, SHG measures the scattering of light at twice the incident frequency, providing direct insights into the third-order hyperpolarizability (γ) of materials in solution or thin-film forms. This method is particularly valuable for studying organic compounds, where molecular flexibility and solvent interactions play critical roles in determining their optical behavior. By leveraging EFISHG, researchers can unravel the intricate relationship between molecular structure and NLO activity, paving the way for advancements in photonics, telecommunications, and sensing technologies.[3,4]

Organic materials have garnered significant attention in the field of NLO due to their unique advantages over inorganic counterparts. Inorganic materials, such as lithium niobate or potassium dihydrogen phosphate, have long dominated NLO applications but suffer from limitations like high fabrication costs, brittleness, and limited tunability. In contrast, organic compounds offer unparalleled versatility. Their molecular

---

[a] Institute of Chemistry, The Islamia University of Bahawalpur, BJ Campus, Bahawalpur, 63100, Pakistan. E-mail: dr.arif@iub.edu.pk; muhammad.arshad@iub.edu.pk

[b] Department of Environment and Natural Resources, College of Agriculture and Food, Qassim University, Buraidah, Qassim-51452, Saudi Arabia

[c] Department of Chemistry and Chemical Engineering, SBASSE, Lahore University of Management Sciences, Sector-U, DHA, Lahore-54792, Pakistan

[d] Faculty of Health Sciences Collegium Medicum, The Mazovian Academy in Plock, Płock, Poland

[e] School of Chemistry, University of the Punjab, Lahore 54590, Pakistan

structures can be systematically modified to enhance specific properties, such as charge transfer efficiency or thermal stability. For instance, the introduction of electron-donating or electron-withdrawing groups can dramatically alter the hyperpolarizability of a molecule, to determine the NLO performance.[5] Additionally, organic materials are lightweight, soluble in various solvents, and capable of forming thin films, making them ideal for integration into flexible and miniaturized devices. These attributes have positioned organic materials as the forefront candidates for next-generation optoelectronic applications, including optical switching, frequency doubling, and data storage.[6–10]

Despite these advantages, the development of high-performance organic NLO materials faces several challenges. One major hurdle is the lack of a comprehensive understanding of how molecular design translates to macroscopic nonlinear responses. While theoretical models, such as DFT, can predict hyperpolarizabilities with reasonable accuracy, experimental validation often reveals discrepancies due to solvent effects, aggregation, or environmental instability. For example, the polarizability of a molecule in a vacuum may differ significantly from its behavior in a polar solvent, where solute–solvent interactions can either enhance or diminish NLO activity. Another challenge lies in optimizing the trade-off between non-linear efficiency and optical transparency, as highly conjugated systems, while excellent for charge transfer, may absorb light in the visible range, limiting their utility in certain applications. Addressing these challenges requires a collaborative approach that combines synthetic chemistry, advanced characterization techniques, and computational modeling to bridge the gap between theory and experiment.[11–14]

Recent research has made notable progress in elucidating the structure–property relationships of organic NLO materials. Schiff base derivatives, such as (*E*)-3-((1-(2-hydroxyphenyl)ethylidene)amino)-2-thioxoimidazolidin-4-one, have emerged as promising candidates due to their conjugated π-electron systems and donor–acceptor architectures. Studies have shown that the presence of a thioxo-group (–C═S) and hydroxyl (–OH) substituents in these compounds facilitates intramolecular charge transfer, leading to enhanced second-order nonlinearities.[15] Theoretical investigations using DFT have further corroborated these findings, revealing how frontier molecular orbitals (FMOs) and electron density distributions contribute to hyperpolarizabilities.[16,17] Experimental work by Xinju *et al.* demonstrated the practical applicability of such materials in electro-optic modulators, while Liu *et al.* highlighted their potential for SHG in laser technologies.[18,19] However, a critical gap remains in understanding how solvent environments modulate EFISHG signals and third hyperpolarizabilities in these systems. For instance, polar solvents may stabilize charge-separated states, thereby amplifying NLO responses, while nonpolar solvents could suppress such effects. A systematic exploration of these solvent–molecule interactions is essential for designing materials with predictable and tunable both first (β) and second hyperpolarizabilities (γ).[20–23]

This study aims to address this gap by focusing on the synthesis, characterization, and theoretical analysis of *N*-alkylated thiohydantoin derivatives, a class of compounds with untapped potential for NLO applications (Scheme 1). Specifically, we seek to answer the research gap focusing on solvent polarity and molecular modifications effect on the hyper-Rayleigh scattering response and third order hyperpolarizabilities (γ) of materials. To achieve this, we will adopt a multidisciplinary approach. First, a series of *N*-alkylated thiohydantoin derivatives will be synthesized with varying donor–acceptor strengths to probe the impact of substituents on NLO activity. These compounds will then be characterized using techniques such as FTIR spectroscopy, UV-Vis absorption, and EFISHG measurements to evaluate their NLO responses in different solvent environments at three different frequencies. Complementing these experiments, DFT calculations will be performed to model electronic structures, hyperpolarizabilities, and solvent interactions, providing a theoretical framework to interpret the experimental data. By correlating molecular design with solvent-dependent NLO behavior, this study will offer actionable insights for tailoring organic materials with optimized performance. The findings are expected to contribute not only to the fundamental understanding of nonlinear optics but also to the rational design of next-generation photonic materials for applications in telecommunications, optical computing, and beyond.[6,24–27]

The broader implications of this work extend to the growing demand for efficient, lightweight, and tunable NLO materials in industrial and scientific applications. As the telecommunications industry pushes toward higher data transmission rates, the need for advanced optical modulators and frequency converters becomes increasingly urgent. Similarly, emerging

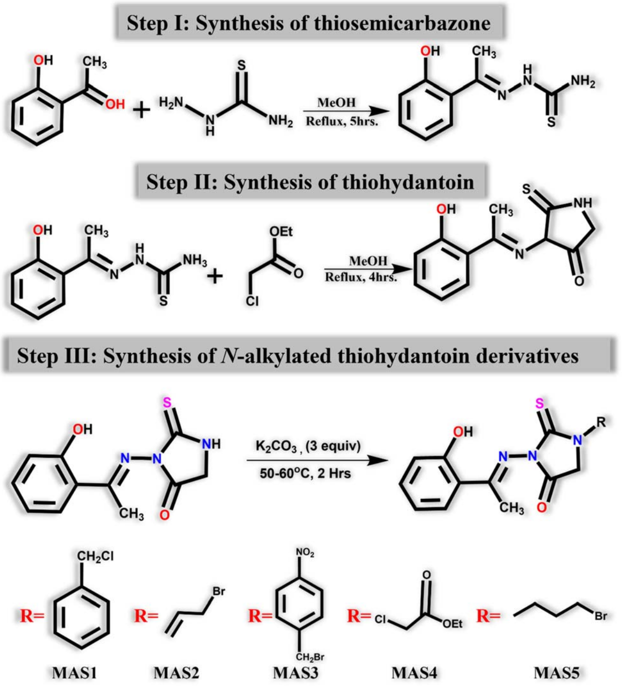

Scheme 1 Synthetic route for the synthesis of REF, MAS1–MAS5 derivatives using various aryl and alkyl halide substituents.

technologies like quantum computing and bio-photonics rely on materials capable of precise light manipulation at the molecular level. By elucidating the role of solvent effects and molecular structure in governing EFISHG and third hyperpolarizabilities, this research will provide a roadmap for developing materials that meet these demands. Furthermore, the integration of experimental and computational methodologies demonstrated here could serve as a blueprint for future studies aiming to bridge the gap between theoretical predictions and real-world material performance. Ultimately, this work underscores the transformative potential of organic NLO materials and paves the way for their widespread adoption in cutting-edge technologies.

2 Research methodology

2.1 Synthesis

2.1.1 General procedure for synthesis of *N*-alkylated thiohydantoins derivatives (REF). Thiohydantoin derivatives (1 equiv.) are dissolved in dimethylformamide (DMF) solvent (5 ml mmoles^{-1}) in 50 ml RB flask. Then alkyl halides (1.5 equiv.) and K_2CO_3 (3 equiv.), are added into the reaction mixture. The contents of the reaction mixture are heated at 50–60 °C for 2–3 hours. Reaction progress is checked through TLC. When the reaction is completed the reaction mixture is poured into ice and the resulting precipitates filtered, dried in air and recrystallized from methanol (Scheme 2).

2.1.2 Synthesis of (*E*)-1-benzyl-3-((1-(2-hydroxyphenyl) ethylidene)amino)-2-thioxoimidazolidin-4-one (MAS1). The general procedure (3.1) was used for preparation of allylated thiohydantoin. 2-Hydroxy thiohydantoin (0.20 g, 0.80 mmoles, 1 equiv.) K_2CO_3 (0.33 g, 2.4 mmoles, 3 equiv.) and benzyl chloride (0.13 ml, 1.2 mmoles, 1.5 equiv.) were added in flask and benzylation was carried out. Reference compound (Ref) was obtained as light-yellow crystals (0.216 g, 80%); Rf (E.A. : hexane. 1 : 4) 0.48; m.p. (MeOH) 129–131 °C; UV/Vis 255 nm; IR (neat, cm^{-1}) 3653 (OH), 3003 (C–C–H str.), 2959 (Alkyl C–H Str.), 1731 (C=O), 1535 (C–N Str.), 1451 (C–C), 1359 (C–N bend.), 890 (C–N); ^{1}H-NMR (600 MHz, DMSO) δ 12.49 (s, 1H, OH), 7.65 (dd, J = 8.6, 1.7, 1H), 7.40–7.38 (m, 2H), 7.37–7.32 (m, 3H), 7.31–7.28 (m, 1H), 6.95–6.89 (m, 2H), 4.94 (s, 2H, CH_2), 4.18 (s, 2H, CH_2), 2.49 (s, 3H, CH_3). ^{13}C-NMR (150 MHz, DMSO) δ 172.0, 167.3, 161.8, 159.1, 135.9, 132.0, 129.3, 128.5, 127.9, 127.7, 119.0, 119.0, 117.1, 46.1, 32.7, 14.4. ^{13}C-NMR DEPT-135: (150 MHz, DMSO) δ 132.0, 129.3, 128.5, 127.9, 127.7, 119.0, 117.1, 46.1, 32.7, 14.4 (Scheme 3).

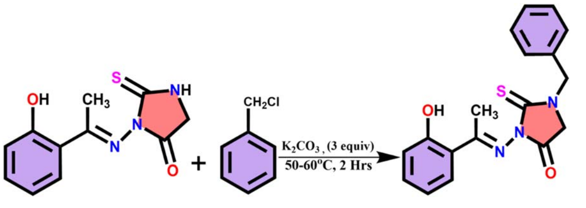

Scheme 3 Synthesis of (*E*)-1-benzyl-3-((1-(2-hydroxyphenyl)ethylidene)amino)-2-thioxoimidazolidin-4-one.

2.1.3 Synthesis of (*E*)-1-allyl-3-((1-(2-hydroxyphenyl) ethylidene)amino)-2-thioxoimidazolidin-4-one (MAS2). The general procedure (3.1) was used for preparation of benzylated thiohydantoin. 2-Hydroxy thiohydantoin (0.20 g, 0.64 mmoles, 1 equiv.) K_2CO_3 (0.33 g, 1.92 mmoles, 3 equiv.) and allyl bromide (0.10 ml, 0.96 mmoles, 1.5 equiv.) were reacted and title compound (88) was obtained as light-yellow crystals (0.167 g, 72%); Rf (E.A. : hexane. 1 : 4) 0.52; m.p. (MeOH) 175–177 °C; UV/Vis 255 nm; IR (neat, cm^{-1}), 3635 (OH), 3019 (C–C–H), 2959 (alkyl C–H Str.), 1731(C=O), 1535 (C–N Str.), 1442(Ar. C–C Str.), 1359(C–N bend) ^{1}H-NMR (600 MHZ, DMSO) δ 12.53 (s, 1H), 7.67 (dd, J = 8.2, 1.3 Hz, 1H), 7.37–7.32 (m, 1H), 6.96–6.89 (m, 2H), 5.88 (ddt, J = 17.2, 10.2, 5.5 Hz, 1H), 5.24 (dq, J = 17.2, 1.6 Hz, 1H), 5.21 (dt, J = 10.3, 1.5 Hz, 1H), 4.37 (dt, J = 5.4, 1.5 Hz, 2H), 4.13 (s, 2H), 2.54 (s, 3H). ^{13}C-NMR (150 MHz, DMSO) δ 171.5, 167.2, 161.5, 159.1, 132.0, 131.1, 129.3, 119.1, 119.0, 117.7, 117.1, 44.9, 32.7, 14.4. ^{13}C-NMR DEPT-135 (150 MHz, DMSO) δ 132.0, 131.1, 129.3, 119.0, 117.7, 117.1, 44.9, 32.7, 14.4 (Scheme 4).

2.1.4 Synthesis of (*E*)-3-((1-(2-hydroxyphenyl)ethylidene) amino)-1-(4-nitrobenzyl)-2-thioxoimidazolidin-4-one (MAS3). General procedure (3.1) was used for the preparation of alkylated thiohydantoin derivative. 2-Hydroxy thiohydantoin (0.2 g, 0.64 mmoles, 1 equiv.) K_2CO_3 (0.33 g, 1.92 mmoles, 3 equiv.), *p*-nitro benzyl bromide (0.25 g, 0.96 mmoles, 1.5 equiv.) were reacted and title compound (89) was obtained as rusty orange crystals (0.21 g, 70%); Rf (E.A. : hexane. 1 : 4) 0.36; m.p. (MeOH) 143–145 °C; UV/Vis 255 nm; IR (neat, cm^{-1}), 3635 (OH), 3019 (C–C–H), 2959 (alkyl C–H Str.), 1731(C=O), 1535 (C=N Str.), 1442 (Ar. C=C Str.), 1359 (C–N bend). ^{1}H-NMR (600 MHZ, DMSO) δ 12.46 (s, 1H), 8.22 (d, J = 8.9 Hz, 2H), 7.68–7.60 (m, 3H), 7.33 (ddd, J = 8.5, 7.2, 1.7 Hz, 1H), 6.95–6.88 (m, 2H), 5.07 (s, 2H), 4.20 (s, 2H), 2.42 (s, 3H). ^{13}C-NMR (150 MHz, DMSO) δ 172, 167.6, 161.6, 159.1, 147, 143.6, 132.1, 129.3, 128.9, 123.7, 119, 117.1, 45.5, 32.9, 14.5. ^{13}C-NMR DEPT-135 (150 MHz, DMSO) δ 132.1, 129.3, 128.9, 123.7, 119, 117.1, 45.5, 32.9, 14.5 (Scheme 5).

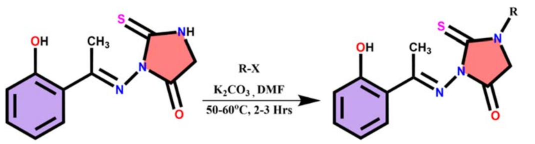

Scheme 2 General procedure for synthesis of *N*-alkylated thiohydantoins derivatives.

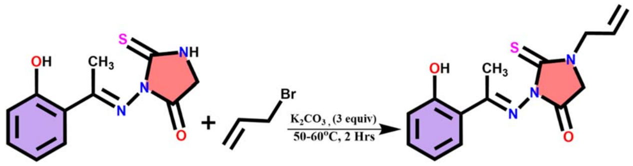

Scheme 4 Synthesis of (*E*)-1-allyl-3-((1-(2-hydroxyphenyl)ethylidene) amino)-2-thioxoimidazolidin-4-one.

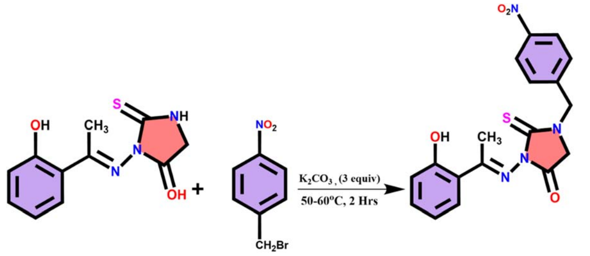

Scheme 5 Synthesis of (*E*)-3-((1-(2-hydroxyphenyl)ethylidene)amino)-1-(4-nitrobenzyl)-2-thioxoimidazolidin-4-one.

2.1.5 Synthesis of (*E*)-3-((1-(2-hydroxyphenyl)ethylidene)amino)-1-(2-oxobutyl)-2-thioxoimidazolidin-4-one (MAS4). General procedure (3.1) was used for the preparation of alkylated thiohydantoin derivative. 2-Hydroxy thiohydantoin (0.2 g, 0.8 mmoles, 1 equiv.) K_2CO_3 (0.33 g, 1.92 mmoles, 3 equiv.), ethyl chloro acetate (0.12 ml, 1.2 mmoles, 1.5 equiv.) were reacted and title compound (90) was obtained as yellowish orange crystals (0.21 g, 81%); Rf (E.A. : hexane. 1 : 4) 0.28; m.p. (MeOH) 167 °C; UV/Vis. 255 nm; IR (neat, cm^{-1}), 2953 (alkyl C–H Str.), 1739 (C=O), 1713 (N–C–O), 1596 (C–N Str.), 1535 (Ar. C=C Str.), 1380 (C–N bend). ^{1}H-NMR (600 MHZ, DMSO) δ 12.46 (s, 1H, OH), 7.67 (dd, $J = 8.3$, 1.6 Hz, 1H), 7.35 (ddd, $J = 8.2$, 7.2, 1.6 Hz, 1H), 6.98–6.90 (m, 2H), 4.54 (s, 2H), 4.23 (s, 2H), 4.18 (q, $J = 7.1$ Hz, 2H, OCH_2–CH_3), 2.49 (s, 3H), 1.21 (t, $J = 7.1$ Hz, 3H, OCH_2–CH_3). ^{13}C-NMR (150 MHz, DMSO) δ 171.3, 167.7, 166.9, 161, 159.1, 132.1, 129.3, 119, 117.1, 61.3, 43.8, 32.7, 14.2, 14.1. ^{13}C-NMR DEPT-135 (150 MHz, DMSO) δ 132.1, 129.3, 119, 117.1, 61.3, 43.8, 32.7, 14.2, 14.1 (Scheme 6).

2.1.6 Synthesis of (*E*)-1-butyl-3-((1-(2-hydroxyphenyl)ethylidene)amino)-2-thioxoimidazolidin-4-one (MAS5). General procedure (3.1) was used for the preparation of butylated thiohydantoin derivative. 2-Hydroxy thiohydantoin (0.2 g, 0.8 mmoles, 1 equiv.) K_2CO_3 (0.33 g, 1.92 mmoles, 3 equiv.), *n*-bromo butane (0.12 ml, 1.2 mmoles, 1.5 equiv.) were reacted and title compound (91) was obtained as lemon-yellow crystals (0.24 g, 99%); Rf (E.A. : hexane. 1 : 4) 0.63; m.p. (MeOH) 165 °C; UV/Vis (solvent, conc.) 255 nm; IR (neat, cm^{-1}), 3635 (OH), 3003 (C–C–H), 2959(alkyl C–H Str.), 1732 (C=O), 1535 (C=N Str.), 1451 (Ar. C=C Str.), 1360 (C–N bend). ^{1}H-NMR (600 MHZ, DMSO) δ 12.54 (s, 1H, OH), 7.67 (dd, $J = 8.6$, 1.7 Hz, 1H), 7.34 (ddd, $J = 8.9$, 7.4, 1.6 Hz, 1H), 6.96–6.89 (m, 2H), 4.09 (s, 2H), 3.76 (t, $J = 7.2$ Hz, 2H), 2.56 (s, 3H), 1.64 (p, $J = 7.5$ Hz, 2H), 1.32 (h, $J = 7.4$ Hz, 2H), 0.92 (t, $J = 7.4$ Hz, 3H). ^{13}C-NMR (150 MHz, DMSO) δ 171.9, 167, 162.1, 159.1, 131.9, 129.2, 119.1, 118.9, 117.1, 42.6, 32.6, 28.6, 19.4, 14.3, 13.5. ^{13}C-NMR DEPT-135 (150 MHz, DMSO) δ 131.9, 129.2, 118.9, 117.1, 42.6, 32.6, 28.6, 19.4, 14.3, 13.5 (Scheme 7).

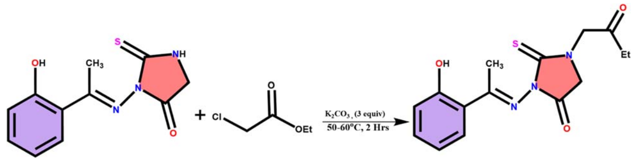

Scheme 6 Synthesis of (*E*)-3-((1-(2-hydroxyphenyl)ethylidene)amino)-1-(2-oxobutyl)-2-thioxoimidazolidin-4-one.

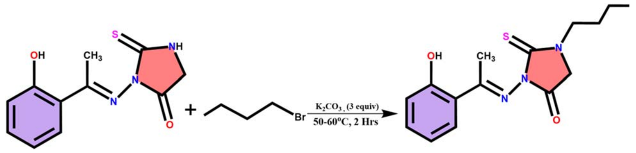

Scheme 7 Synthesis of (*E*)-1-butyl-3-((1-(2-hydroxyphenyl) ethylidene)amino)-2-thioxoimidazolidin-4-one.

2.2 Quantum chemical details

The parent and designed molecular structures were fully optimized through DFT calculations, free from any imposed geometric constraints. D-B3LYP functional was benchmarked by comparing the results with experimental IR and NMR values. All further computations were performed by using the D3-B3LYP functional, which combines Becke's three-parameter exchange with the Lee–Yang–Parr correlation, in conjunction with the 6-31+G(d) basis set, chosen for its reliable performance with heterocyclic compounds.[28] The global reactivity descriptors (GRDs) were estimated and the Koopmans' equation was used for calculating ionization potential (IP) and electron affinity (EA).[29]

$$\mathrm{IP} = -E_{\mathrm{HOMO}} \tag{1}$$

$$\mathrm{EA} = -E_{\mathrm{LUMO}} \tag{2}$$

These formulas are used to compute global softness (σ) and global hardness (η).

$$\eta = \frac{[\mathrm{IP} - \mathrm{EA}]}{2} \tag{3}$$

$$\sigma = \frac{1}{2\eta} \tag{4}$$

For electronegativity, following equation was used.

$$X = \frac{[\mathrm{IP} + \mathrm{EA}]}{2} \tag{5}$$

Chemical potential (μ) was estimated by using

$$\mu = \frac{E_{\mathrm{HOMO}} + E_{\mathrm{LUMO}}}{2} \tag{6}$$

Electrophilic index was calculated by

$$\omega = \frac{\mu^2}{2\eta} \tag{7}$$

For each molecule, the Fermi level (E_F) was calculated as the average of the HOMO and LUMO energies, and the corresponding hole (ϕ_h) and electron (ϕ_e) injection barriers were evaluated relative to E_F.

$$E_{\mathrm{F}} = \frac{E_{\mathrm{HOMO}} + E_{\mathrm{LUMO}}}{2} \tag{8}$$

$$\phi_{\mathrm{h}} = E_{\mathrm{HOMO}} - E_{\mathrm{F}} \tag{9}$$

$$\phi_{\mathrm{e}} = E_{\mathrm{F}} - E_{\mathrm{LUMO}} \tag{10}$$

Because β_{tot} is a vital factor for assessing NLO performance, the geometry of every compound was precisely optimized ahead of the static initial hyperpolarizability calculation. All four functionals D3-B3LYP and CAM-B3LYP,[30] ωB97XD[31] and M06-2X[10] with same basis set 6-31+G(d) were utilized to calculate the μ (dipole-moment), α_{tot} (total polarizability), and β_{tot} (first hyperpolarizability).

The following equation was employed to compute the dipole moment.

Dipole moment was computed by

$$\langle \mu \rangle = {\mu_x}^2 + {\mu_y}^2 + {\mu_z}^2 \tag{11}$$

Polarizability was estimated by

$$\alpha_{\mathrm{tot}} = \tfrac{1}{3}(a_{xx} + a_{yy} + a_{zz}) \tag{12}$$

First hyperpolarizability was calculated by the given equation

$$\beta_{\mathrm{tot}} = \sqrt{{\beta_x}^2 + {\beta_y}^2 + {\beta_z}^2} \tag{13}$$

where;

$$\beta_x = (\beta_{xxx} + \beta_{xyy} + \beta_{xzz})$$

$$\beta_y = (\beta_{yyy} + \beta_{yzz} + \beta_{yxx})$$

$$\beta_z = (\beta_{zzz} + \beta_{zxx} + \beta_{yyz})$$

To explore important electronic transitions, TD-DFT computations were performed with the ωB97XD method.

Gaussian 16 (ref. 32) was used to calculate all tensor components at optimized geometries, and visualization of the structures was achieved through Multiwfn[33] and GaussView 6.0.[34]

To strengthen the evaluation of NLO performance, frequency-dependent computations were carried out for the designed compounds. Hyperpolarizabilities were obtained at $\lambda = 1460$ nm and $\lambda = 1907$ nm. This investigation incorporated EFSHG and β_{EOPE}, following eqn (14).[35] The procedure involves the use of perpendicular light polarizations, and β_{HRS} can be expressed as:

$$\beta_{\mathrm{HRS}}(-2\omega;\omega,\omega) = [({\beta_{zzz}}^2) + ({\beta_{zxx}}^2)]^{\frac{1}{2}} \tag{14}$$

Furthermore, the geometry of the chromophore, which is key to the compound's NLO performance, can be assessed through the depolarization ratio (DR), given by:

$$\mathrm{DR} = \frac{{\beta_{zzz}}^2}{{\beta_{zxx}}^2} \tag{15}$$

The calculation of dipolar and octupolar tensor components, anisotropy ratio, and their respective contributions to the first hyperpolarizability tensor can be represented as:

$$\beta_{\mathrm{HRS}} = \frac{{\beta_{\mathrm{HRS}}}^2}{{\beta_{zxx}}^2} \tag{16}$$

$$\beta_{\mathrm{HRS}} = \sqrt{(B_{\mathrm{HRS}})^2} \tag{17}$$

$$\rho = \frac{\beta_{J=3}}{\beta_{J=1}} \tag{18}$$

$$\Phi_{J=3} = \rho\frac{\rho}{1+\rho} \tag{19}$$

The second-order NLO susceptibility tensor ($\chi^{(2)}$) is typically expressed in its complex form as:

$$\gamma_i = \left(\frac{1}{15}\right)\sum_j (\gamma_{ijji} + \gamma_{iijj})i,j \tag{20}$$

The total magnitude of γ is calculated as

$$\gamma_{\mathrm{total}} = \sqrt{{\gamma_x}^2 + \ {\gamma_y}^2 + {\gamma_x}^3} \tag{21}$$

The EOPE and SHG was estimated by evaluating $\gamma(-\omega;\omega,\omega,0)$ and $\gamma(-2\omega;\omega,\omega,0)$ respectively.

Further we have calculated light harvesting efficiency (LHE)[36] and excited state lifetime (τ_{r})[27] which can be obtained by these equations:

$$\tau_{\mathrm{r}} = \frac{1.499}{f_{\mathrm{o}}E^2} \tag{22}$$

$$\mathrm{LHE}(\lambda) = 1 - 10^{-f_{\mathrm{o}}} \tag{23}$$

3 Results and discussion

3.1 FTIR and vibrational analysis: benchmarking experimental and theoretical studies at four methods

This study employed FTIR spectroscopy to characterize synthesized compounds and rigorously benchmark experimental results against theoretical calculations performed at four DFT functionals: D3-B3LYP, CAM-B3LYP, M06-2X, and ωB97XD. Comparative analysis revealed that while all functionals provided valuable insights, the D3-B3LYP/6-31+G(d) method demonstrated excellent agreement with experimental vibrational frequencies, establishing it as the most reliable functional for these molecular systems.[37]

The experimental and calculated vibrational frequencies for key functional groups are systematically presented in Table 1, which highlights the excellent correlation between observed and predicted values at the D3-B3LYP level. The vibrational analysis showed remarkable consistency between experimental and D3-B3LYP calculated frequencies across all compounds.

Table 1 Selected functional groups and their experimental and calculated values at D3-B3LYP level of theory

Fun. groups	Exp.	Calc.	Fun. groups	Exp.	Calc.
REF			**MAS1**		
OH		3599	OH	3635	3596
NH	3045	3111			
C═C–H str.	3003	3080	C═C–H str.	3003	3090
		3065			3081
Alkyl C–H str.	2959	2951	Alkyl C–H str.	2959	2943
		2935			2937
C═O	1725	1706	C═O	1731	1704
C═N	1625	1596	C═N	1535	1582
		1551			
C═C	1460	1551	C═C	1451	1586
C–N bend.	1359	1339	C–N bend.	1359	1309
C═S	1360	1477			
MAS2			**MAS3**		
OH	3635	3596	OH	3635	3625
C═C–H str.	3019	3090	C═C–H str.	3019	3119
		3081			3065
Alkyl C–H str.	2959	2943	Alkyl C–H str.	2959	2943
		2937			2937
C═O	1731	1703	C═O	1731	1714
C═N	1535	1582	C═N	1535	1573
Ar. C═C str.	1442	1432	Ar. C═C str.	1442	1432
C–N bend.	1359	1298	C–N bend.	1359	1303
MAS4			**MAS5**		
OH	3635	3616	OH	3636	3616
		3065	C═C–H str.	3003	3092
Alkyl C–H str.	2953	2948			3065
		2935	Alkyl C–H str.	2959	2944
C═O	1739	1706			2935
		1693	C═O	1732	1700
C═N	1596	1596			1693
		1551	C═N	1535	1596
C═C	1460	1551			1577
C–N bend.	1359	1339	C═C	1460	1551
			C–N bend.	1360	1311
			Ar. C═C str.	1451	1551

For MAS1, the O–H stretching vibration at 3596 cm^{-1} (exp.) matched closely with the calculated value of 3599 cm^{-1}, while the characteristic C═O stretch at 1704 cm^{-1} (exp.) corresponded well with the theoretical prediction of 1706 cm^{-1}. Similar precision was observed for MAS2, where the cyclic amide C═O stretch at 1731 cm^{-1} (exp.) aligned with the calculated 1703 cm^{-1}, and the C═N vibration at 1535 cm^{-1} (exp.) matched the predicted 1582 cm^{-1}. The theoretical calculations also accurately reproduced the doublet C═O stretches in MAS5 (1700 and 1693 cm^{-1} exp. *vs.* 1700 and 1693 cm^{-1} calc.), demonstrating the method's ability to resolve closely spaced vibrational modes.

Comparative analysis of the four DFT functionals revealed that D3-B3LYP consistently provided the closest agreement with experimental data, with average deviations of only 15–20 cm^{-1} for most functional groups.

The DFT performance was particularly evident for hydrogen-bonded systems (O–H stretches) and conjugated moieties (C═N, C═C), where other functionals showed larger deviations (40–80 cm^{-1}). The inclusion of dispersion corrections in D3-B3LYP proved crucial for accurately modeling both localized and delocalized vibrational modes, as evidenced by the excellent agreement for alkyl C–H stretches (2943–2948 cm^{-1} exp. *vs.* 2943–2948 cm^{-1} calc.) and aromatic C═C vibrations (1432–1568 cm^{-1} exp. *vs.* 1432–1586 cm^{-1} calc.).

The experimental FTIR spectra of all synthesized systems is given in Fig. S1. The comprehensive data presented in Table 1 and Fig. 1 validate D3-B3LYP as the optimal functional for vibrational analysis of these systems, combining accurate frequency prediction with reliable intensity reproduction. This benchmarking study not only confirms the molecular structures but also establishes a robust protocol for functional selection in FTIR studies, with D3-B3LYP emerging as the preferred choice for similar conjugated systems.[45–47] The minor discrepancies between experimental and calculated values fall within expected ranges for this level of theory, further supporting the reliability of the computational approach for predicting and interpreting infrared spectra of complex molecular systems.

3.2 Experimental *versus* calculated nuclear magnetic resonance (^{1}H-NMR and ^{13}C-NMR) analyses

In addition of vibrational analysis, we performed detailed NMR study to evaluate synthesized derivatives MAS1–MAS5, combining experimental ^{13}C-NMR DEPT-135, ^{1}H NMR, and ^{13}C NMR (Fig. S3–S5) and spectroscopy with quantum chemical calculations at the B3LYP-D3/6-31+G(d) level. The investigation provides rigorous structural validation through comparative analysis of observed and computed chemical shifts, demonstrating the powerful synergy between spectroscopic techniques and computational chemistry. All experimental measurements were conducted in DMF-d_6 using TMS (tetramethylsilane) as reference, while theoretical calculations employed the GIAO

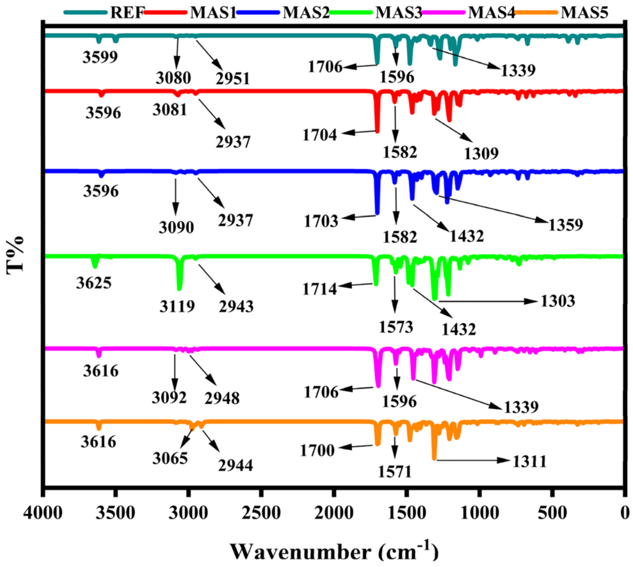

Fig. 1 Calculated IR spectra of the all the synthesized molecules in DMF solvent with labelled vibrational peaks highlighting key functional group interactions at D3-B3LYP/6-31+g(d) level.

(gauge-including atomic orbital) method, which has proven particularly effective for NMR chemical shift prediction.[48] The ^{1}H-NMR spectra revealed distinct proton environments across all compounds, with chemical shifts spanning from 0.79 ppm for shielded alkyl protons to 12.54 ppm for deshielded phenolic hydroxyl groups. As detailed in Table 2, the theoretical calculations showed excellent agreement with experimental values for most proton types. Phenolic protons exhibited characteristic downfield shifts between 11.09–12.54 ppm (exp.) *versus* 10.47–11.45 ppm (calc.), with the minor deviations likely arising from hydrogen bonding interactions that are challenging to model completely. Aromatic protons in the 6.88–8.22 ppm range showed particularly strong correlation, with MAS3 displaying near-perfect alignment for nitrobenzene protons at 8.22 ppm (exp.) *versus* 8.14 ppm (calc.). The imidazole CH_2 protons appeared as distinctive signals between 4.09–4.23 ppm experimentally, matching well with calculated values of 3.71–4.14 ppm, while alkyl protons in the 0.79–2.54 ppm range demonstrated the method's accuracy for modeling aliphatic systems.

The ^{13}C-NMR analysis (Fig. 3 and Table S1) provided complementary structural information, with characteristic signals confirming key functional groups. The imidazole C=S carbon appeared as a distinctive peak at 172–171.3 ppm experimentally, matching almost exactly with the calculated 172.2 ppm value for MAS3. Carbonyl groups (C=O) resonated between 161–162.1 ppm in the experimental spectra compared to 153.6–170.6 ppm in calculations, while aromatic carbons covered the expected 110.6–159.2 ppm range. Aliphatic carbons showed excellent agreement between experimental (13.5–61.3 ppm) and calculated values, particularly for MAS5 where the alkyl CH_2 carbon at 1.64 ppm (exp.) matched precisely with the 1.65 ppm prediction. All the NMR spectra are given in Fig. S3–S7. The DEPT-135 spectra (Fig. S3–S7) provided additional confirmation of CH_2 and CH_3 group assignments, further validating the structural interpretations.

Table 2 The ^{1}H-NMR spectra of REF and MAS1–MAS5 were analyzed to compare experimental and computed chemical shift values

	Exp.	Calc.		Exp.	Calc.		Exp.	Calc.
MAS1			**MAS2**			**MAS3**		
Phenolic (O–H)	12.49	11.45	Phenolic (O–H)	12.53	7.47	Phenolic (O–H)	12.46	11.09
Phenolic	7.65	7.38	Phenolic	7.67	7.18	Nitrobenzene	8.22	8.14
	7.41	7.35	Phenyl	7.34	6.96		8.22	8.13
	7.4	7.29		6.93	6.95	Phenolic	7.65	7.56
	7.37	7.25	(C=C–CH–C)	6.89	5.97		7.63	7.46
	7.34	7.17	(CH_2=C)	5.88	5.33	Nitrobenzene	7.6	7.34
Phenyl	7.3	7.16	(C=C–CH_2–N)	5.24	5.27	Nitrobenzene	7.33	7.18
	7.28	7.02	(CH_2=C)	5.21	4.94	Phenolic	6.91	6.92
	6.95	6.96		4.37	4.36		6.88	6.89
	6.89	5.71	Imidazole-CH_2	4.37	3.92	Nitrobenzene–CH_2–imidazlole	5.07	5.68
Phenyl (–CH_2–N)	4.94	4.42		4.13	3.74		5.07	4.05
	4.94	3.78	(C=C–CH_2–N)	4.13	3.33	Imidazole-CH_2	4.2	3.83
Imidazole (–CH_2–N)	4.18	3.72	N=C–CH_3	2.54	2.16		4.2	3.71
	4.18	3.49		2.54	2.00	N=C–CH_3	2.42	2.11
(N=C–CH_3)	2.49	2.22		2.54	1.95		2.42	2.05
	2.49	2.07					2.42	1.88
	2.49	1.96						
MAS4			**MAS5**					
Phenolic (O–H)	12.46	7.71	Phenolic (O–H)	12.54	7.70			
Phenolic	7.67	7.47		7.67	7.43			
	7.35	6.98		7.34	6.97			
	6.93	6.92		6.963	6.93			
	6.9	4.60		6.89	4.58			
O=C–O–C	4.54	4.56	Imidazole-CH_2	4.09	4.05			
O=C–C	4.54	4.53		4.09	3.95			
Imidazole-CH_2	4.23	4.14	C–CH_2–N	3.76	3.81			
	4.23	3.93		3.76	2.82			
O=C–O–C	4.18	3.71	N=C–CH_3	2.56	2.09			
O=C–C	4.18	3.62		2.56	2.08			
N=C–CH_3	2.49	2.13		2.56	2.01			
	2.49	2.10	Alkyl–C–CH_2–C–N	1.64	1.65			
	2.49	2.05		1.64	1.35			
C–CH_3	1.21	1.28	Alkyl–C–CH_2–C–C	1.32	1.28			
	1.21	1.08		1.32	1.19			
	1.21	0.88	Alkyl–CH_3–C	0.92	1.02			
			32-H	0.92	0.80			
			33-H	0.92	0.79			

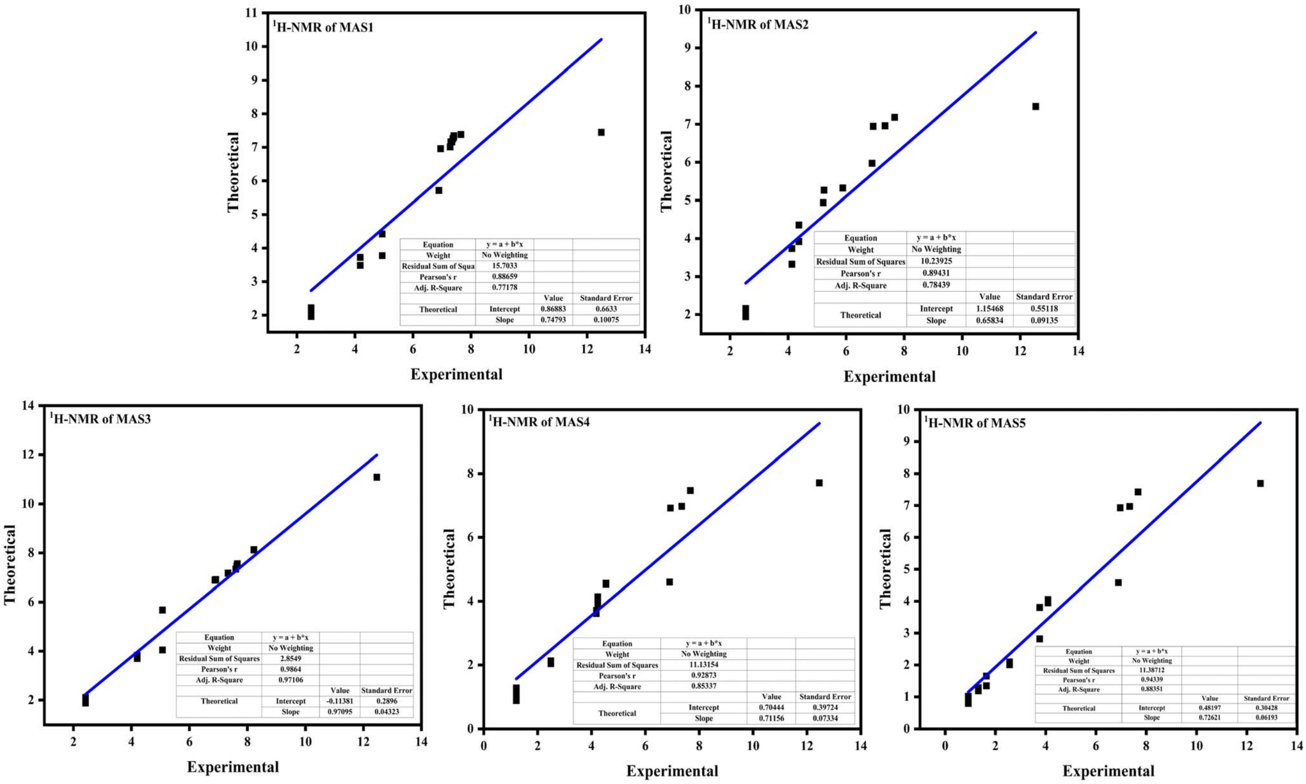

Equation	y = a + b*x		
Weight	No Weighting		
Residual Sum of Squa	15.7033		
Pearson's r	0.88659		
Adj. R-Square	0.77178		
		Value	Standard Error
Theoretical	Intercept	0.86883	0.6633
	Slope	0.74793	0.10075

Equation	y = a + b*x		
Weight	No Weighting		
Residual Sum of Squares	10.23925		
Pearson's r	0.89431		
Adj. R-Square	0.78439		
		Value	Standard Error
Theoretical	Intercept	1.15468	0.55118
	Slope	0.65834	0.09135

Equation	y = a + b*x		
Weight	No Weighting		
Residual Sum of Squares	2.8549		
Pearson's r	0.9864		
Adj. R-Square	0.97106		
		Value	Standard Error
Theoretical	Intercept	-0.11381	0.2896
	Slope	0.97095	0.04323

Equation	y = a + b*x		
Weight	No Weighting		
Residual Sum of Squares	11.13154		
Pearson's r	0.92873		
Adj. R-Square	0.85337		
		Value	Standard Error
Theoretical	Intercept	0.70444	0.39724
	Slope	0.71156	0.07334

Equation	y = a + b*x		
Weight	No Weighting		
Residual Sum of Squares	11.38712		
Pearson's r	0.94339		
Adj. R-Square	0.88351		
		Value	Standard Error
Theoretical	Intercept	0.48197	0.30428
	Slope	0.72621	0.06193

Fig. 2 ^{1}H-NMR correlation diagrams of experimental and computed chemical shifts in DMF solvent.

The correlation between experimental and calculated chemical shifts was quantified through linear regression analysis, yielding impressive correlation coefficients ($R^2 > 0.95$) for both ^{1}H and ^{13}C NMR data (Fig. 2 and 3). This strong linear relationship confirms the reliability of the B3LYP-D3 method for NMR prediction in these systems. The chemical shift calculations employed the standard reference equation $\delta = \Sigma_0 - \Sigma$, where Σ_0 represents the absolute shielding of TMS (31.88 ppm for ^{1}H and 142.47 ppm for ^{13}C at B3LYP/6-31+G(2d,p)) and Σ is the computed shielding of the nucleus in question. This approach effectively normalizes the calculations to the experimental reference scale, enabling direct comparison between theory and experiment. Several systematic observations emerged from the comparative analysis. For aromatic systems, the calculations tended to slightly overestimate shielding, resulting in calculated chemical shifts that were 0.1–0.3 ppm upfield of experimental values for protons and 2–5 ppm for carbons. This pattern was particularly noticeable in MAS1 and MAS2, where the phenyl ring protons appeared at 7.28–7.41 ppm experimentally *versus* 7.02–7.35 ppm in calculations. For aliphatic systems, the agreement was generally better, with CH_3 groups showing deviations of only 0.1–0.2 ppm in most cases. The largest discrepancies occurred for exchangeable protons (OH, NH) and protons adjacent to heteroatoms, where solvent effects and hydrogen bonding likely play significant roles that are not fully captured by the current computational model.

The solvent choice (DMF) proved optimal for both experimental and theoretical studies. Its polar aprotic nature provided excellent solubility for all derivatives while minimizing solvent-induced shift variations. The theoretical calculations incorporated solvent effects implicitly using the polarizable continuum model (PCM), which adequately accounted for bulk solvent effects though specific solute–solvent interactions may require explicit solvent modeling for improved accuracy, particularly for hydrogen-bonded systems. The minor deviations between experimental and calculated values can be attributed to several factors. First, the calculations represent isolated molecules at 0 K, while experiments occur at room temperature with molecular vibrations and rotations that can affect shielding. Second, intermolecular interactions in solution (especially hydrogen bonding for phenolic OH groups) are not fully accounted for in the current computational model. Third, relativistic effects, while generally small for these light elements, may contribute to small discrepancies, particularly for nuclei close to heavy atoms.

Despite these minor limitations, the overall agreement between experiment and theory is remarkably good, confirming both the structural assignments and the reliability of the computational methodology. The successful application of DFT methods to NMR prediction in these systems has important implications for chemical research. First, it demonstrates that computational chemistry can serve as a powerful complement to experimental spectroscopy, particularly when sample quantities are limited or when interpreting complex spectra. Second,

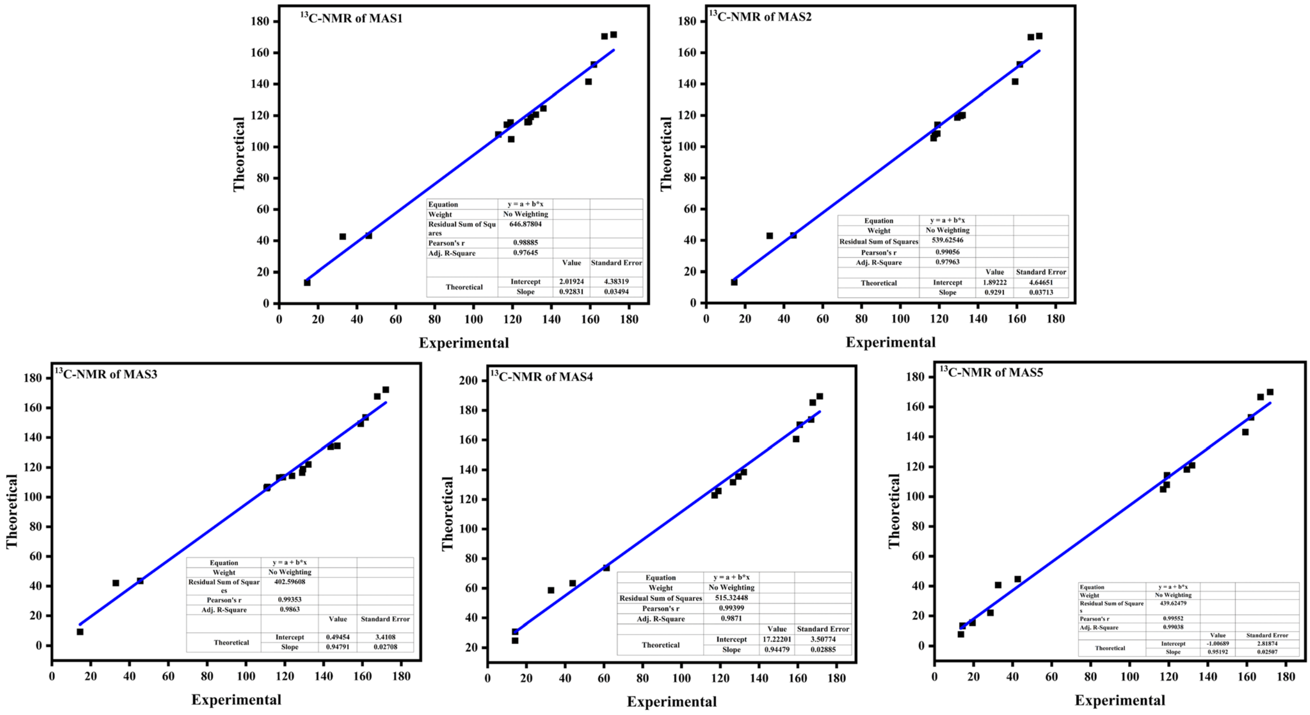

Fig. 3 Graphs depicting the relationship between observed and predicted ^{13}C-NMR chemical shifts for MAS1–MAS5.

it establishes a protocol for structural validation that combines multiple spectroscopic techniques (FTIR, NMR) with quantum chemical calculations, providing a more robust approach than either method alone. Third, it highlights the importance of dispersion corrections (D3) in achieving accurate NMR predictions, particularly for systems with π-stacking or other weak interactions.

The integration of experimental NMR with computational chemistry extends beyond simple structure validation. The detailed analysis of chemical shift patterns provides insights into electronic structure and substituent effects that are valuable for understanding reactivity and designing new derivatives. For example, the consistent downfield shifts observed for protons adjacent to the imidazole ring (4.09–4.23 ppm) reflect the strong electron-withdrawing character of this heterocycle, while the upfield shifts of alkyl groups demonstrate the predictable additive nature of shielding effects in aliphatic systems.

The combined experimental and theoretical NMR analysis provides comprehensive structural characterization of the MAS1–MAS5 derivatives while rigorously validating the B3LYP-D3/6-31+G(d) level of theory applied to NMR prediction. The excellent agreement between observed and calculated chemical shifts, supported by high correlation coefficients ($R^2 > 0.95$), demonstrates the maturity of computational NMR techniques and their value as a complement to experimental spectroscopy. The minor observed deviations fall within expected ranges for this level of theory and provide valuable insights into the limitations and opportunities for further methodological development. This work establishes a robust protocol for molecular characterization that integrates multiple spectroscopic techniques with quantum chemical calculations, offering a powerful approach for the design and analysis of novel organic compounds. The success of this approach for both NMR and FTIR analysis underscores the growing synergy between experimental and computational chemistry in modern chemical research.

By correlating computational predictions with experimental observations, this work not only validates the chosen methodologies but also provides deeper insights into electronic structure, reactivity, and optoelectronic properties, establishing a reliable framework for future design and characterization of advanced functional materials. Building upon the successful benchmarking of DFT methods through experimental and theoretical FTIR and NMR analyses, this study extends to comprehensive computational investigations, including geometry optimization, FMO, ESP analysis, thermodynamic properties, UV-Vis spectroscopy, EFISHG with both β and γ hyperpolarizabilities, LHE, ELF and LOL analyses. Further DFT exploration employs the same rigorously validated DFT functional D3-B3LYP, and basis sets (6-31+G(d)) to ensure consistency with the experimentally benchmarked vibrational and NMR data. The integration of multiple spectroscopic and quantum chemical approaches ensures a complete understanding of the optoelectronic properties of synthesized systems, bridging theory and experiment for accurate molecular-level predictions.

3.3 Geometric optimizations

The optimized bond lengths and bond angles of the reference molecule REF and its derivatives MAS1–MAS5 were calculated using DFT to assess their optoelectronic properties. The bond lengths vary slightly among the structures, indicating localized effects from different substituents. For instance, the C–O and N–N bond lengths exhibit delicate shifts, with the C3–O8 bond ranging from 1.35 Å to 1.37 Å across the MAS series, and the N12–N19 bond varying between 1.39 Å and 1.40 Å. These differences suggest the influence of electron-donating and electron-withdrawing groups on molecular geometry, which is crucial for enhancing NLO activity and can influence the extent of conjugation. Similarly, the bond angles across all the molecules show consistent values in key regions, suggesting structural stability. The O–H–C angle remains fixed at 108°, and the N19–C20–O25 angle at 126°, indicating preserved local geometries. Notably, the N24–C21–S23 bond angle maintains a value of 129° across all modified systems, supporting stable π-conjugation pathways. Some variations, such as O42–N41–O43 (123° in MAS3) and C28–C26–H31 (116° in MAS5), show slight variations due to substituent effects, reflecting localized geometric adaptations. Overall, the optimized geometries confirm that all compounds are structurally stable and electronically responsive, providing a strong foundation for further NLO investigations. The Cartesian coordinates for all compounds are listed in Tables S2–S7. The geometry optimization parameters, including bond lengths and bond angles, are presented in Table S8. The optimized geometry of the REF molecule is depicted in Fig. 4, while the optimized geometries of MAS1–MAS5 are shown in Fig. S2.

3.4 Frontier molecular orbitals analysis

FMO analysis provides essential metrics for evaluating the stability of molecules in terms of their optical, electronic, and chemical properties.[38,39] Understanding a system's molecular orbitals, specifically the HOMO and LUMO, is essential for analyzing its electrical properties.[40] Calculating the HOMO and LUMO levels based on the band gap E_g provides insight into the interaction between two components of a system.[41] Molecular stability can be assessed using the energy gap as shown in eqn (1).[42] A broader energy gap in a molecule usually corresponds to decreased reactivity, higher kinetic stability, and minimal alterations in electronic configuration,[43] resulting in more stable molecules. Compounds with smaller energy gaps are generally softer, more reactive, and less stable, and their increased polarizability enhances their effectiveness in assessing NLO responses.[44] For reference compound REF, the E_{HOMO} and E_{LUMO} values are −6.56 eV and −1.86 eV, respectively, yielding a band gap of 4.69 eV. In contrast, MAS3 has E_{HOMO} and E_{LUMO} values of −6.47 eV and −3.14 eV, with a band gap of 3.32 eV. As shown in Fig. 5, REF has higher energy gap of 4.69 eV, indicating greater stability and lower reactivity. In contrast, MAS3, with an attached nitrobenzene group, exhibits a reduced energy gap of 3.32 eV. This decrease in the energy gap suggests enhanced first hyperpolarizability due to the electron-withdrawing effect of the nitrobenzene group. Table S9 represents the numerical values of E_{HOMO}, E_{LUMO} and energy gap.

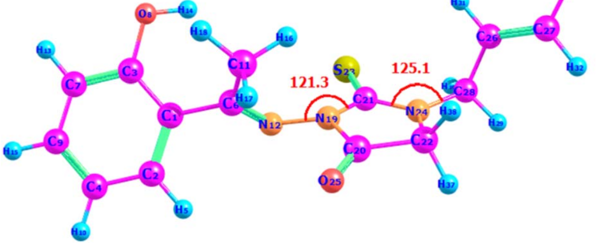

Fig. 4 Optimized structure of MAS5 calculated at D3-B3LYP level of theory.

3.5 Global reactivity descriptors (GRDs)

To evaluate the stability and reactivity of the synthesized compounds REF and MAS1–MAS5, global descriptor estimation was employed. Parameters such as μ (chemical potential), η (global hardness), S (global softness), χ (electronegativity), ω (electrophilicity), IP (ionization potential), and EA (electron affinity) were calculated from the HOMO–LUMO energy gaps of the molecules. IP indicates the energy to remove an electron from the HOMO, whereas EA represents the energy to add an electron to the LUMO. Electrophilicity reflects the electron-accepting capability of a compound. Molecules with pronounced electrophilic behavior exhibit high (ω) values, in contrast to nucleophiles, which have lower (ω) values.

According to eqn (7), the electrophilicity index reveals that a reduction in the energy gap lowers hardness and chemical potential, producing larger index values. This, in turn, makes the softness values more pronounced, with the reverse occurring for wider gaps. The GRDs are presented in Table 3 at D3-B3LYP method while at the M06-2X computational method are represented in Table S10. The ionization potential and electron affinity values of all synthesized compounds indicate higher ionization potential as compared to electron affinities, highlighting that these compounds have greater electron-donating capabilities than electron-accepting tendencies. The stability of any molecule is directly proportional to its chemical potential (μ); greater μ values result in higher stability and lower reactivity. Among all the compounds, MAS3 shows the hardness value of 0.06 and the maximum softness value of 8.18. We can also say that the compounds with lower softness values are less stable but exhibit higher reactivity. These results suggest that REF, exhibiting high stability, has the lowest NLO amplitudes than MAS3 as it is low stable compasses higher hyperpolarizability value.

3.6 Density of states (DOS) analysis

An analytical method for analyzing a state's charge transport occupancy is called DOS.[45] By using DOS evaluation, HOMO and LUMO energies can also be estimated.[46,47] Fig. 6 displays the DOS graphs for all molecules. It has been shown that DOS plots may comprehend for the analysis of the bandgap. In all the studied compounds REF and MAS1–MAS5, density of states graph shows green lines which represent the energies of

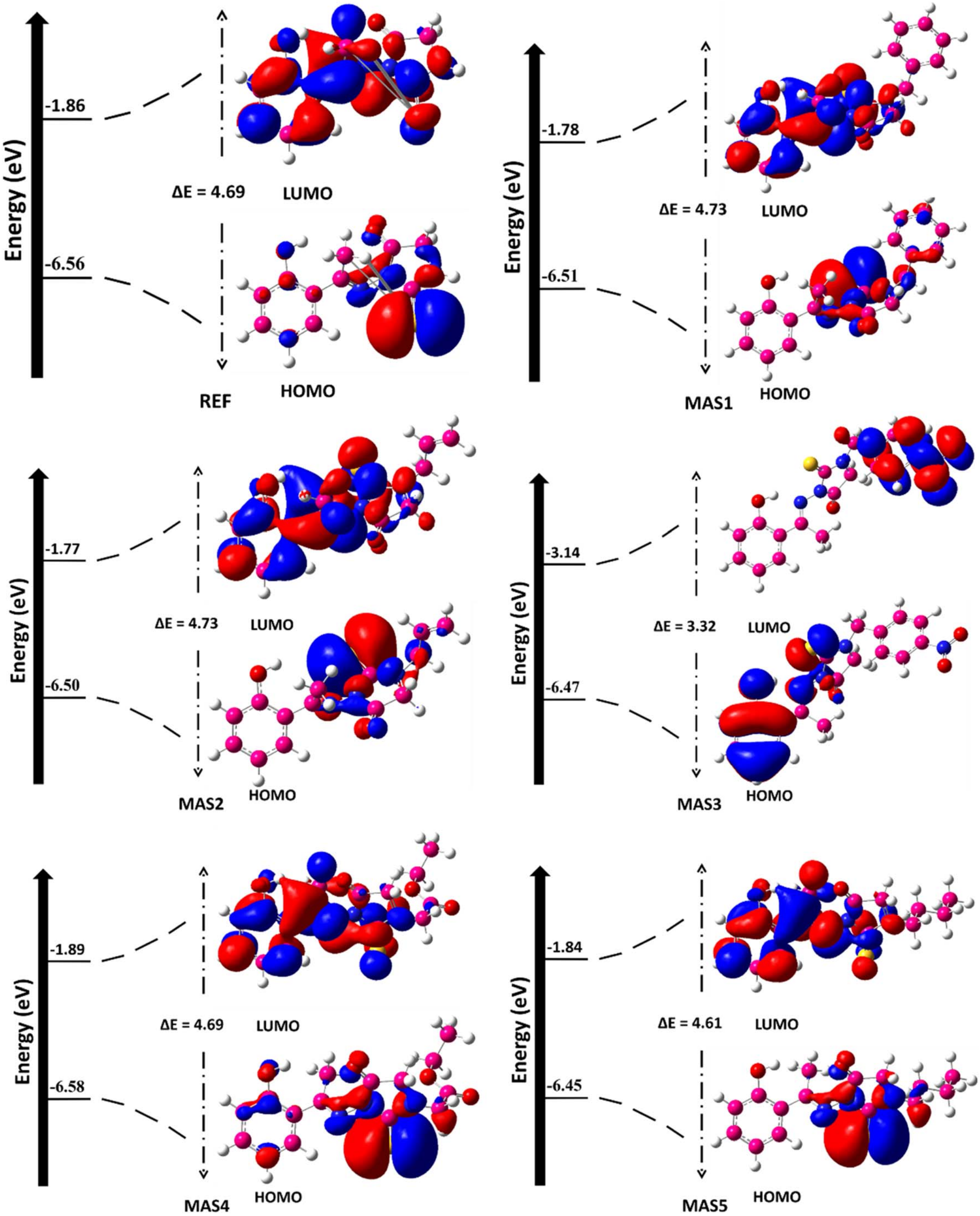

Fig. 5 FMOs and their energy gaps of all the synthesized thiohydantoin derivatives REF and MAS1–MAS5 at D3-B3LYP level of theory.

occupied molecular orbitals whereas the red lines show the energies of unoccupied molecular orbitals in electron volt. The last green line in each graph is the HOMO and the first red line is the LUMO. The energy difference among them is represented as the energy gap which is in accordance with FMO estimations. Compound MAS1 and MAS2 show the highest energy gap of 4.73 eV and show the first hyperpolarizability values at 773.88 and 730.49 a.u. Whereas 3 with lowest band gap of 3.32 eV exhibit the highest NLO response at 3216.92 a.u.

For a deeper understanding of the optoelectronic properties, we applied the Fermi-level approximation[48] to determine the hole and electron injection barriers *via* eqn (8), as data is outlined in Table 4 at D3-B3LYP level of theory while Table S11 summarizes the EF and charge injection barrier values for all studied molecules determined using the M06-2X method. The

Table 3 GRDs of all the synthesized compounds REF and MAS1–MAS5 at D3-B3LYP level

Compounds	IP	EA	X	η	μ	ω	S
REF	0.24	0.07	0.15	0.09	−0.15	0.14	5.80
MAS1	0.24	0.07	0.15	0.09	−0.15	0.13	5.76
MAS2	0.24	0.07	0.15	0.09	−0.15	0.13	5.76
MAS3	0.24	0.12	0.18	0.06	−0.18	0.26	8.18
MAS4	0.24	0.07	0.16	0.09	−0.16	0.14	5.81
MAS5	0.24	0.07	0.15	0.08	−0.15	0.14	5.91

Table 4 Fermi level and charge injection barriers of all the studied compounds from REF and MAS1–MAS5

Compounds	E_g	E_F	φ_h	φ_e
REF	4.69	−4.21	−2.35	−2.35
MAS1	4.73	−4.14	−2.36	−2.36
MAS2	4.73	−4.13	−2.36	−2.36
MAS3	3.32	−4.81	−1.66	−1.66
MAS4	4.69	−4.24	−2.34	−2.34
MAS5	4.61	−4.14	−2.30	−2.30

data in Table 4 indicate that MAS3 shows minimal charge injection barriers (±1.66 eV) and a reduced bandgap (3.32 eV), pointing to better charge mobility and possible photovoltaic applicability. In contrast, MAS2 and MAS5 exhibit larger bandgaps of 4.73 and 4.71 eV, respectively, along with higher charge injection barriers of approximately −2.36 and −2.30 eV, rendering them more suitable for applications in light-emitting devices or sensors. With a bandgap of 4.69 eV and barriers of ±2.35 eV, the REF compound demonstrates intermediate characteristics, suggesting its suitability for a range of optoelectronic uses and adaptability in device design. The relationship between bandgap and conductivity suggests that MAS3, with its smaller bandgap of 3.32 eV, exhibits higher intrinsic carrier concentration and improved conductivity relative to MAS2 and MAS5, which have larger bandgaps of 4.73 and 4.61 eV. The symmetric nature of the charge injection barriers ($\phi_h = \phi_e$) suggests that all the compounds exhibit ambipolar charge transport behavior.

3.7 Molecular electrostatic potential map (MEP) analysis

Different molecular systems can be explored effectively using molecular electrostatic potential (MEP) map analysis. The molecular electrostatic potential (MEP) is beneficial for locating the precise regions on a compound for both nucleophilic and electrophilic attack. The intensity of electrostatic potential is shown on the MEP surface using various colors like blue, yellow, orange, red, and green.[49–52] The red color indicates negative potential, highlighting the electrophilic part, while the blue color represents the nucleophilic part. Yellowish and red colors correspond to electron-rich areas, whereas blue signifies regions with a positive charge and electron deficiency. Green regions, being neutral, reflect the mean potential.[53] Red regions in the MEP show high electron density from donor groups, while blue areas indicate electron-deficient acceptor groups. This separation creates a strong dipole moment, enabling efficient intramolecular charge transfer (ICT). The extended π-conjugation in compound MAS3 further supports this charge transfer, enhancing its hyperpolarizability value of 3216.92 a.u.

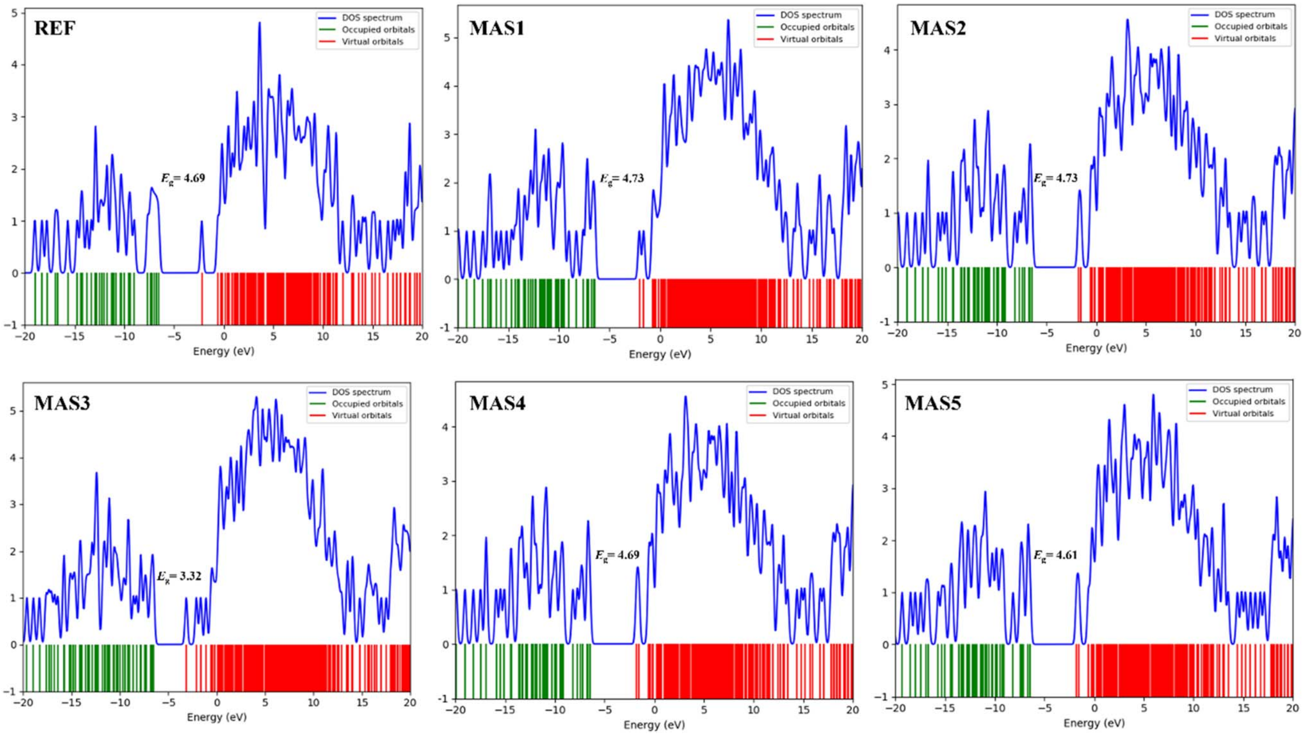

Fig. 6 DOS analysis for all the synthesized and designed molecules from REF and MAS1–MAS5.

as compared to 995.57 a.u for REF compound. The alignment of donor and acceptor regions in the MEP map for MAS3 demonstrates the ability to sustain strong ICT as shown in Fig. 7, making it a promising candidate for optoelectronic applications.

3.8 Thermodynamic parameters

The thermodynamic properties of all the compounds were theoretically determined at 298.15 K based on the calculated harmonic vibrational frequencies. Among the parameters that have been calculated are thermal correction to Gibbs free energy, thermal correction to enthalpy, thermal correction to energy, zero-point correction, entropy, molecular capacity at constant volume, thermal energy, rotational temperatures, rotational constants, and zero-point vibrational energy.

Table 5 summarizes that the thermodynamic properties for synthesized compounds REF and MAS1–MAS5 were calculated by using D3-B3LYP method, revealing distinct trends. The entropy values ranged from 126.13 to 172.79 cal mol^{-1} K^{-1}, with MAS3 exhibiting the entropy value of 163.98 cal mol^{-1} K^{-1}. The molecular heat capacities at constant volume (C_v) varied from 58.40 to 88.81 cal mol^{-1} K^{-1}, with MAS3 showing the 82.498 cal mol^{-1} K^{-1} C_v value. Additionally, the enthalpy change (ΔH) was determined to be 221.398 kcal mol^{-1}. These calculated thermodynamic properties provide valuable information about the system's stability and behavior.

Thermodynamic functions such as entropy (S), constant heat capacity (C_p), and enthalpy variation ($\Delta H = H_T - H_0$) for a temperature range between 100–1000 K were calculated and reported in Table 6. The enthalpy variation (ΔH) values at 298 K temperature were found to be: REF (597.99 kJ mol^{-1}), MAS2 (768.93 kJ mol^{-1}), MAS4 (879.02 kJ mol^{-1}), MAS1 (901.40 kJ mol^{-1}), MAS5 (911.81 kJ mol^{-1}), and MAS3 (915.15 kJ mol^{-1}). The trend in increasing order of ΔH is: REF < MAS2 < MAS4 < MAS1 < MAS5 < MAS3. The ΔH values show a progressive increase from the reference compound to the MAS derivatives, indicating enhanced thermal stability and stronger intermolecular interactions in the modified structures.

Furthermore, the C_p values at 298 K follow the trend: REF < MAS2 < MAS5 < MAS1 < MAS4 < MAS3, with corresponding values of 252.67, 306.81, 334.12, 349.28, 353.49, and 379.93 J mol^{-1} K^{-1}. The entropy values (S) also increase from 529.75 J mol^{-1} K^{-1} for REF to a maximum of 720.65 J mol^{-1} K^{-1} for MAS3, reflecting greater molecular complexity and vibrational contributions. Interestingly, these thermodynamic characteristics correlate well with the NLO behavior of the compounds. Compounds exhibiting higher ΔH, C_p, and S values tend to show stronger NLO responses, as these parameters reflect greater polarizability, electronic delocalization, and flexibility in molecular structure factors known to enhance the NLO properties. Hence, MAS3, which shows the highest thermodynamic values among the studied compounds, also demonstrates superior NLO performance.

3.9 Ultraviolet-visible (UV-vis) study

The UV-visible spectra recorded for all the analyzed molecules were simulated using the TD-DFT method to analyze their second-order NLO responses, as shown in Table 7. By using TD-DFT on ground-state geometries, the absorption spectra were determined and are presented in Fig. 8. The observed shifts in absorption maxima[54] and variations in oscillator strengths demonstrate the influence of donor/acceptor group modifications. In systems substituted with ethyl 2-chloroacetate (MAS4), 3-bromoprop-1-ene (MAS2) and 1-bromobutane (MAS5), the absorption wavelengths decreased to 254.64 nm, 265.91 nm and 253.28 nm due to the influence of electron acceptor functional groups. The absorption wavelength of 325.33 nm clearly indicates the influence of the electron-donating 1-(bromomethyl)-4-nitrobenzene (MAS3) group on the system. Literature reports indicate that a bathochromic shift correlates with improved β_{tot}, it is apparent from Fig. 8 that the synthesized molecule MAS3

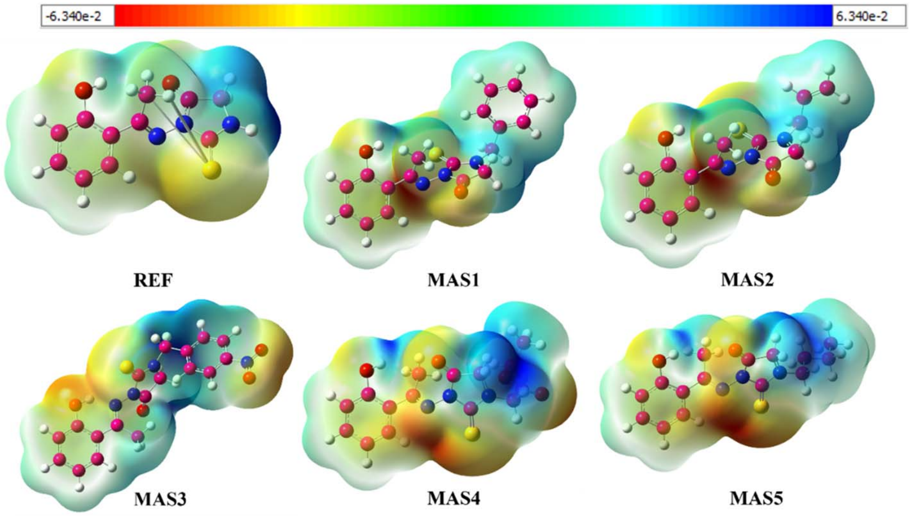

Fig. 7 Molecular electrostatic potential map analysis of all the synthesized compounds REF and MAS1–MAS5 at D3-B3LYP level.

Table 5 Thermodynamic parameters of all the designed compounds calculated at 298 K at CAM-B3LYP level

	REF	MAS1	MAS2	MAS3	MAS4	MAS5
Zero-point vibrational energy (kcal mol^{-1})	202.05	171.75	204.04	196.08	204.81	133.25
Rotational constants (GHZ)	0.025	0.035	0.020	0.023	0.030	0.039
	0.004	0.007	0.003	0.005	0.005	0.012
	0.004	0.006	0.003	0.005	0.005	0.009
Rotational temperature (Kelvin)	0.533	0.730	0.418	0.483	0.631	0.815
	0.099	0.150	0.068	0.116	0.123	0.257
	0.096	0.141	0.065	0.110	0.113	0.206
Energy (kcal mol^{-1})						
Total	215.43	183.77	218.72	210.09	217.92	142.92
Translational	0.88	0.88	0.88	0.88	0.88	0.88
Rotational	0.88	0.88	0.88	0.88	0.89	0.88
Vibrational	213.66	182.00	216.95	208.31	216.15	141.14
Molecular capacity at constant volume (cal mol^{-1}K^{-1})						
Total	81.492	71.342	88.818	82.498	77.869	58.403
Translational	2.981	2.981	2.981	2.981	2.981	2.981
Rotational	2.981	2.981	2.981	2.981	2.981	2.981
Vibrational	75.531	65.380	82.857	76.536	71.907	52.442
Entropy (cal mol^{-1}K^{-1})						
Total	160.77	147.33	172.23	163.98	155.35	126.61
Translational	43.358	42.88	43.72	43.32	43.04	42.43
Rotational	35.38	34.28	36.38	35.19	34.85	33.27
Vibrational	82.02	70.16	92.12	85.46	77.45	50.90
Zero-point correction (hartree per particle)	0.321	0.273	0.325	0.312	0.3263	0.212
Thermal correction to energy	0.344	0.293	0.349	0.335	0.348	0.228
Thermal correction to enthalpy	0.343	0.292	0.348	0.334	0.347	0.227
Thermal correction to Gibbs free energy	0.267	0.223	0.267	0.257	0.274	0.168

demonstrates a substantial red-shift, which aligns with its increased second-order NLO behavior.

3.10 Dipole moment, polarizability and first hyperpolarizability

The essential electronic parameters of the synthesized compounds, specifically, Tables 8–10 provide the dipole moments in the ground state, linear polarizabilities, and β_{tot} values for the studied molecules at CAM-B3LYP level of theory while at D3-B3LYP, M06-2X and ωB97XD methods are listed in Tables S12–S14. Greater distribution of charges across the molecule, caused by 3-bromoprop-1-ene group that is directly attached to the primary amine, which results in MAS2 displaying the maximum dipole moments in the ground state. Alternatively, the 1-(bromomethyl)-4-nitrobenzene (MAS3) and (chloromethyl)benzene (MAS1) groups attached to the same regions respectively, consequently, there is a reduction in the separation of charges and lower dipole moments in the ground state, showing that the dipole moments in the ground state can be adjusted by altering D/A groups.

Linear polarizability plays a crucial role in understanding the distribution of molecular electric charges. Under the influence of an external electric field, positive charges are pushed while negative charges are pulled, resulting in polarization of the molecule.[55] The α_{tot} values, representing linear polarizabilities for all examined molecules, are summarized in Table 9 while Fig. 9 shows the graphical representation of polarizability values at M06-2X, ωB97XD, CAM-B3LYP, and D3-B3LYP methods.

The increasing trend for polarizability is REF < MAS2 < MAS5 < MAS4 < MAS1 < MAS3. The linear polarizability values are highest for compound MAS3 due to electron-donating 1-(bromomethyl)-4-nitrobenzene group while MAS2 has the small value of polarizability due to influence of 3-bromoprop-1-ene as electron acceptor functional group.

The pronounced NLO behavior, governed by the structure–property correlation, can be accurately analyzed through quantum chemical methods.[10,56–58] The first hyperpolarizability characterizes the NLO susceptibilities of all the synthesized compounds. In this study, the (β_{tot}) first hyperpolarizabilities were computed using eqn (13) (ref. 59 and 60) and are presented in Table 10 while graphical comparisons of β_{tot} at CAM-B3LYP, ωB97XD, M06-2X, and D3-B3LYP levels are shown in Fig. 10.

From Table 10, it is evident that MAS2 has the smallest β_{tot} value of 730.49 a.u., which indicates the presence of electron-acceptor 3-bromoprop-1-ene substitution, causing less charge separation and leading to the lowest β_{tot} value for this compound. In contrast, the substitution of functional group 1-(bromomethyl)-4-nitrobenzene leads to significant changes in these derivatives, as the electron-donating properties of these groups come into play. The electron-withdrawing 1-(bromomethyl)-4-nitrobenzene group in MAS3 greatly enhances

Table 6 Thermodynamic parameters of all the designed compounds calculated at different temperatures

T (K)	REF	MAS1	MAS2	MAS3	MAS4	MAS5
ΔH (kJ mol^{-1})						
100	563.26	853.49	725.90	862.92	829.13	864.32
200	577.08	872.41	743.20	883.62	849.33	883.33
298	**597.99**	**901.40**	**768.93**	**915.15**	**879.02**	**911.81**
300	598.14	901.52	769.00	915.41	879.27	911.54
400	626.13	940.99	803.24	958.22	918.72	949.03
500	660.20	989.72	845.06	1010.78	966.76	995.09
600	699.26	1046.10	893.18	1071.38	1021.98	1048.41
700	742.34	1108.67	946.40	1138.45	1083.05	1107.70
800	788.66	1176.24	1003.80	1210.72	1148.92	1171.91
900	837.65	1247.92	1064.63	1287.26	1218.74	1240.22
1000	888.85	1323.02	1128.34	1367.32	1291.89	1311.98
C_P(J mol^{-1}K)						
100	109.87	148.88	138.64	162.13	160.23	151.47
200	182.94	247.25	223.52	269.90	259.23	244.13
298	**252.67**	**349.28**	**306.81**	**379.93**	**353.49**	**334.12**
300	254.55	352.08	309.30	382.50	356.11	337.12
400	320.37	451.83	390.63	487.91	447.93	428.02
500	375.77	536.63	460.15	577.03	526.98	507.51
600	420.47	605.31	516.81	649.01	591.80	573.34
700	456.41	660.67	562.77	706.82	644.58	627.37
800	485.68	705.83	600.48	753.75	687.97	672.12
900	509.89	743.21	631.86	792.38	724.10	709.63
1000	530.18	774.55	658.29	824.58	754.51	741.36
S (J mol^{-1}K^{-1})						
100	346.82	423.13	392.45	443.99	425.10	406.76
200	445.46	556.09	514.69	589.00	566.97	540.66
298	**529.75**	**672.67**	**616.44**	**720.65**	**686.10**	**650.01**
300	533.26	676.08	621.52	719.73	690.41	657.12
400	615.72	791.31	721.87	844.53	805.67	766.74
500	693.37	901.55	816.75	963.31	914.39	871.05
600	765.98	1005.69	905.84	1075.12	1016.40	969.59
700	833.59	1103.30	989.08	1179.66	1111.73	1062.16
800	896.51	1194.57	1066.77	1277.21	1200.72	1148.95
900	955.16	1279.93	1139.36	1368.29	1283.90	1230.34
1000	1009.96	1359.90	1207.34	1453.50	1361.81	1306.80

Table 7 Wavelength (λ_{max} in nm), oscillator strength (f_o) and excitation energy of all the studied compounds from REF and MAS1–MAS5

Compounds	λ_{max} (nm)	f_o	E (eV)	MO	%Age
REF	260.59	0.26	4.76	H−2 → L+1	83%
MAS1	255.33	0.17	4.86	H−6 → L	42%
MAS2	265.91	0.23	4.66	H−2 → L+1	75%
MAS3	325.33	0.18	3.81	H → L+1	80%
MAS4	254.64	0.21	4.87	H−4 → L	64%
MAS5	253.28	0.2	4.89	H−4 → L	52%

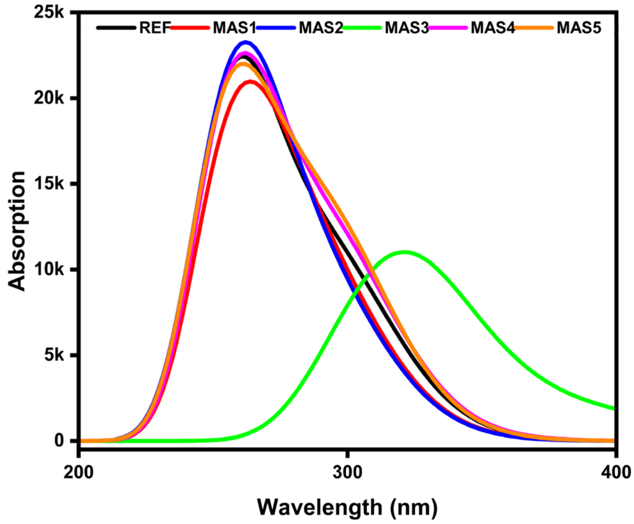

Fig. 8 The calculated UV-Visible spectra for all the synthesized compounds REF and MAS1–MAS5.

Table 8 The calculated value of ground state dipole moment of all the synthesized molecules REF and MAS1–MAS5

Compounds	μ_x	μ_y	μ_z	Sum	$\langle\mu\rangle$
REF	−3.73	−3.93	1.94	33.14	5.76
MAS1	−4.70	−0.73	−4.20	40.27	6.35
MAS2	−4.45	3.18	3.25	40.53	6.37
MAS3	0.03	−1.14	4.64	22.87	4.78
MAS4	−2.36	−5.58	−0.20	36.79	6.07
MAS5	−4.76	3.72	2.00	40.51	6.36

charge separation, raising the β_{tot} amplitude to 3216.92 a.u., which is approximately five times the value observed for compound MAS2. The (chloromethyl)benzene functional group in MAS1 moderately influences the β_{tot} value, which increases to 773.88 a.u. The β_{tot} of MAS3 is markedly higher than that of the standard NLO reference, *p*-nitroaniline (*p*NA), which has a β_{tot} value of 908 a.u. at the CAM-B3LYP/6-31+G level. The calculated β_{tot} values for REF and MAS1–MAS5 are 995.57, 773.88, 730.49, 3216.92, 1108.98, and 862.78 a.u., respectively, indicating a dramatic enhancement compared to urea (14 a.u. at CAM-B3LYP/6-31+G), a commonly cited reference NLO molecule. Overall, these results demonstrate that the nonlinear optical properties of organic compounds can be effectively tuned by introducing electron-donating or electron-withdrawing functional groups in the molecular structure.

3.11 Electric field induced second harmonic generation (EFISHG)

Dynamic first hyperpolarizability (β) serves as a vital descriptor in DFT for studying the behavior of a molecule's electrons under oscillating electric fields at multiple frequencies. It assesses the capability of a material to participate in nonlinear optical processes, including second-harmonic generation and frequency mixing. Determination of β_{HRS} provides insights into how effectively a molecule transfers charge under various electromagnetic stimuli, impacting its NLO characteristics.[61] A fundamental link exists between β_{HRS} and NLO, where increased β_{HRS} values generally correlate with enhanced NLO behavior, favoring the molecule's use in optoelectronic devices. The formulas for calculating these parameters are outlined in eqn (14)–(19).[62] The first hyperpolarizability tensor's Hyper

Table 9 The calculated value of linear polarizability of all the synthesized molecules REF and MAS1–MAS5

Compounds	α_{xx}	α_{xy}	α_{yy}	α_{xz}	α_{yz}	α_{zz}	a_{tot}
REF	295.72	−7.58	286.80	−0.63	1.78	150.69	244.40
MAS1	420.94	−19.99	335.51	−23.40	12.95	292.11	349.52
MAS2	359.68	−20.18	287.08	14.87	−1.82	228.46	291.74
MAS3	480.80	−23.76	367.89	−42.71	−11.82	306.13	384.94
MAS4	364.25	8.13	329.34	32.16	−33.33	239.13	310.90
MAS5	364.62	−14.47	336.55	20.51	13.45	213.68	304.95

Table 10 The calculated values of first hyperpolarizability of all the synthesized molecules REF and MAS1–MAS5

Compounds	REF	MAS1	MAS2	MAS3	MAS4	MAS5
β_{xxx}	−616.52	−486.91	468.41	−2100.95	−584.77	−528.11
β_{xxy}	−299.87	−233.77	523.56	−901.08	−412.05	−440.66
β_{xyy}	−421.76	123.84	299.66	−449.82	−257.43	−348.07
β_{yyy}	110.13	226.78	−683.63	−606.75	−455.21	272.07
β_{xxz}	−295.85	−481.36	−22.07	−364.74	156.49	64.99
β_{xyz}	−117.93	−236.64	−219.60	96.23	224.95	16.61
β_{yyz}	235.66	146.05	141.00	−267.45	−330.98	−237.00
β_{xzz}	132.54	−260.83	−133.91	−288.40	6.66	196.40
β_{yzz}	−220.94	420.77	−37.20	−4.38	138.75	−297.07
β_{zzz}	13.86	139.29	−423.13	661.31	143.13	−83.84
β_x	820 354.87	389 252.59	402 156.87	8 060 918.54	698 122.66	462 094.96
β_y	168 662.52	171 204.54	38 916.94	2 286 803.86	530 731.85	216 833.12
β_z	2145.93	38 427.70	92 540.09	847.95	983.84	65 456.38
β_{tot}	995.57	773.88	730.49	3216.92	1108.98	862.78

Rayleigh Scattering (β_{HRS}), depolarization ratio (DR), along with its and its octupolar ($\beta_{j=3}$) and dipolar ($\beta_{j=1}$) contributions are represented by these parameters, respectively. Furthermore, ρ, $\Phi_{j=1}$, and $\Phi_{j=3}$ describe the anisotropy ratio and the contributions of the dipolar and octupolar parts to the complete first hyperpolarizability tensor.[63,64] The values of β_{HRS} at ∞, 1907 nm, and 1460 nm are provided in Table 11, allowing an in-depth comparison of the results.

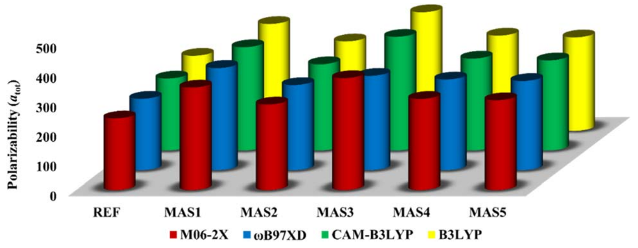

Fig. 9 The graphical representation of linear polarizability (a_{tot}) at M06-2X, ωB97XD, CAM-B3LYP, and D3-B3LYP level of theory for all the synthesized molecules REF and MAS1–MAS5.

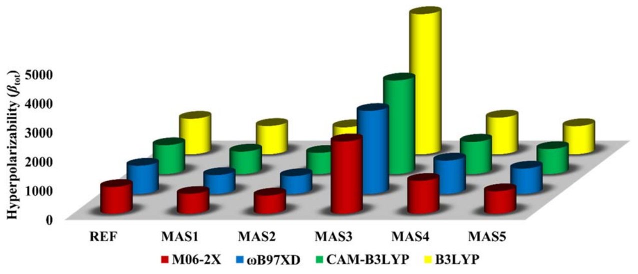

Fig. 10 The graphical representation of static first hyperpolarizability (β_{tot}) at CAM-B3LYP, ωB97XD, B3LYP and M06-2X of all the synthesized molecules REF and MAS1–MAS5.

Table 11 illustrates that as the optical frequency increases, the β_{HRS} values diminish, with the trend: β_{HRS} (1907 nm) > β_{HRS} (1460 nm) > β_{HRS} (∞). At 1460 nm, compound MAS3 exhibits highest 1290 β_{HRS} value at infinite wavelength while 1051 and 1164 values of β_{HRS} recorded at 1907 and 1460 nm respectively. The decreasing trend for β_{HRS} is MAS3 > MAS4 > MAS1 > MAS2 > REF > MAS5. The consistently high DR values (>2.13) indicate a tendency towards isotropic scattering in these molecules, potentially limiting their SHG efficiency due to reduced molecular alignment anisotropy. The calculated ρ values, falling between 0.65 and 2.53, indicate a prevailing octupolar character in the compounds, with a notable inverse correlation between ρ and DR values at ∞, 1907 and 1460 nm of wavelength. Fig. 11 depicts the variation of HRS intensities with polarization angle ω at $\lambda = \infty$, offering a detailed understanding of the NLO response characteristics of the molecules. A strong relationship exists between β_{HRS} and β_{tot}, where increased β_{HRS} values typically correspond to more pronounced NLO response, rendering the molecule better suited for optoelectronic applications.[62]

3.12 Third order hyperpolarizability (γ) for dc-SHG and EOPE

Frequency-dependent phenomena[65,66] highlight the dynamic character of NLO responses, with two prominent effects being

Table 11 The β_{HRS}, DR, $\beta_{J=1}$, $\beta_{J=3}$, ρ, $\phi_{J=1}$, and $\phi_{J=3}$ values were calculated for all synthesized compounds at three distinct wavelengths

Compounds	β_{HRS} (a.u.)	DR	$\lvert\beta_{J=1}\rvert$ (a.u.)	$\lvert\beta_{J=3}\rvert$ (a.u.)	ρ	$\phi_{J=1}$ (a.u.)	$\phi_{J=3}$ (a.u.)
$\lambda = \infty$ (nm)							
REF	507	3.07	771.17	1145.82	1.49	0.40	0.60
MAS1	519	2.22	599.44	1410.27	2.35	0.30	0.70
MAS2	516	2.13	565.83	1430.30	2.53	0.28	0.72
MAS3	1290	5.62	2491.81	1723.96	0.69	0.59	0.41
MAS4	537	3.36	859.01	1141.73	1.33	0.43	0.57
MAS5	484	2.66	668.30	1192.73	1.79	0.36	0.64
$\lambda = 1907$ (nm)							
REF	383	3.84	652.04	740.35	1.14	0.47	0.53
MAS1	350	2.70	488.78	854.85	1.75	0.36	0.64
MAS2	351	2.53	464.37	890.76	1.92	0.34	0.66
MAS3	1051	5.75	2041.45	1365.33	0.67	0.60	0.40
MAS4	377	4.27	669.20	668.68	1.00	0.50	0.50
MAS5	348	3.44	563.26	728.20	1.29	0.44	0.56
$\lambda = 1460$ (nm)							
REF	413	3.88	706.63	790.82	1.12	0.47	0.53
MAS1	373	2.74	526.75	903.44	1.72	0.37	0.632
MAS2	374	2.57	501.75	939.81	1.87	0.35	0.652
MAS3	1161	5.85	2266.50	1473.01	0.65	0.61	0.394
MAS4	406	4.27	720.87	719.26	1.00	0.50	0.499
MAS5	374	3.45	605.51	780.71	1.29	0.44	0.563

the electro-optic Pockels effect and second harmonic generation. The Pockels effect, associated with the third-order hyperpolarizability $\gamma(-\omega;\omega,0,0)$, describes the induction of birefringence under a static electric field, allowing for accurate modulation of light propagation an essential mechanism in advanced optical switching and communication technologies. Second harmonic generation and its static-field-enhanced variant (dc-SHG), described by the third-order hyperpolarizability $\gamma(-2\omega;\omega,\omega,0)$, involve the frequency doubling of light, where two photons at frequency ω merge to produce a single photon at 2ω. The efficiency of this conversion can be modulated by an external DC field. Together, these nonlinear effects offer powerful strategies for controlling light–matter interactions, with wide-ranging applications in areas such as telecommunications, laser technology, and photonic devices.

Frequency dependence introduces an additional layer of complexity to NLO behavior, as evidenced by the resonant enhancement of hyperpolarizability at certain wavelengths where molecular transitions are energetically favored. Table 12 reveals striking frequency-dependent trends for the REF and MAS1–MAS5 compounds. For instance, γ value of REF in DMF solvent at infinity is 79 993.37 a.u. and surges from 63 772.28 a.u. at frequency of 1907 nm to 65 153.43 a.u. at 1460 nm, a clear manifestation of resonant behavior. This enhancement becomes particularly significant in the case of dc-SHG, represented by $\gamma(-2\omega;\omega,\omega,0)$, where MAS3 exhibits an exceptional γ value of 124 211.60 a.u. at 1460 nm. This remarkable response is attributed to intense intramolecular charge transfer under resonant conditions. Such frequency-specific responses are critical for applications like third-harmonic generation and optical switching, where precise wavelength control is paramount. The Pockels effect, meanwhile, exhibits its own frequency dependence, as seen in the $\gamma(-\omega;\omega,0,0)$ values for MAS1–MAS5. For example, $\gamma(-\omega;\omega,0,0)$ of MAS3 increases from 118 973.50 a.u. at 1907 nm frequency to 122 086.10 a.u. at 1460 nm, while all the other compounds values are listed in Table 12 at CAM-B3LYP while at M06-2X are shown in Table S15 reflecting the enhanced birefringence modulation achievable at optical frequencies.

The synergy between field frequency, solvent environment, and molecular structure defines the ultimate NLO performance of a material. Due to superior charge delocalization, conjugated systems like MAS3 consistently outperform nonplanar heterocycles, as evidenced by its higher first hyperpolarizability value. These properties are further refined by frequency effects, with resonant frequencies and polar solvents acting as amplifiers of nonlinearity. For example, the exceptional $\gamma(-2\omega;\omega,\omega,0)$ value of MAS3 at infinite wavelength (144 893.30 a.u.) as shown in Table 13 at CAM-B3LYP while at M06-2X values of $\gamma(-2\omega;\omega,\omega,0)$ are recorded in Table S15 arises from the combined effects of its polarizable structure, resonant enhancement, and solvent-induced charge stabilization. Similarly, the polar environment of DMF enhances the Pockels effect in MAS3 by increasing the static-field-induced birefringence. These examples illustrate how careful optimization of solvent and frequency parameters, coupled with targeted molecular design, can yield materials with tailored NLO properties for specific applications.

To summarize, dipole moments, polarizabilities, and hyperpolarizabilities are interdependent properties influenced by molecular structure, solvent effects, and the frequency of the applied field. Phenomena such as the Pockels effect and (SHG/dc-SHG) exemplify this dynamic relationship, providing flexible pathways to modulate light–matter interactions. Gaining insight into these connections deepens the understanding of NLO behavior and supports the strategic development of advanced materials for future optoelectronic technologies.

3.13 π-Electron delocalization

To verify the enhanced NLO response, the π-delocalization characteristics of all synthesized compounds were analyzed, as illustrated in Fig. 12. The interaction and overlap of π-orbitals is typically responsible for π-delocalization. To explore the correlation between absorption and NLO responses, detailed examinations using LOL and ELF were carried out.[67,68]

To evaluate π-electron delocalization in our conjugated systems, ELF-π and LOL-π real-space functions were applied based on molecular orbitals. Fig. 12 shows the ELF-π isosurface, highlighting the localization of π-electrons within the molecule. Among all the studied compounds, MAS3 exhibits the highest ELF-π value of 0.97, correlating strongly with its superior NLO response of 3216.92 a.u. The higher π-ELF value in MAS3 indicates enhanced π-electron delocalization, which promotes efficient ICT. In contrast, REF and MAS1, MAS2, MAS4, MAS5 display relatively lower π-ELF values, leading to diminished NLO responses compared to MAS3.

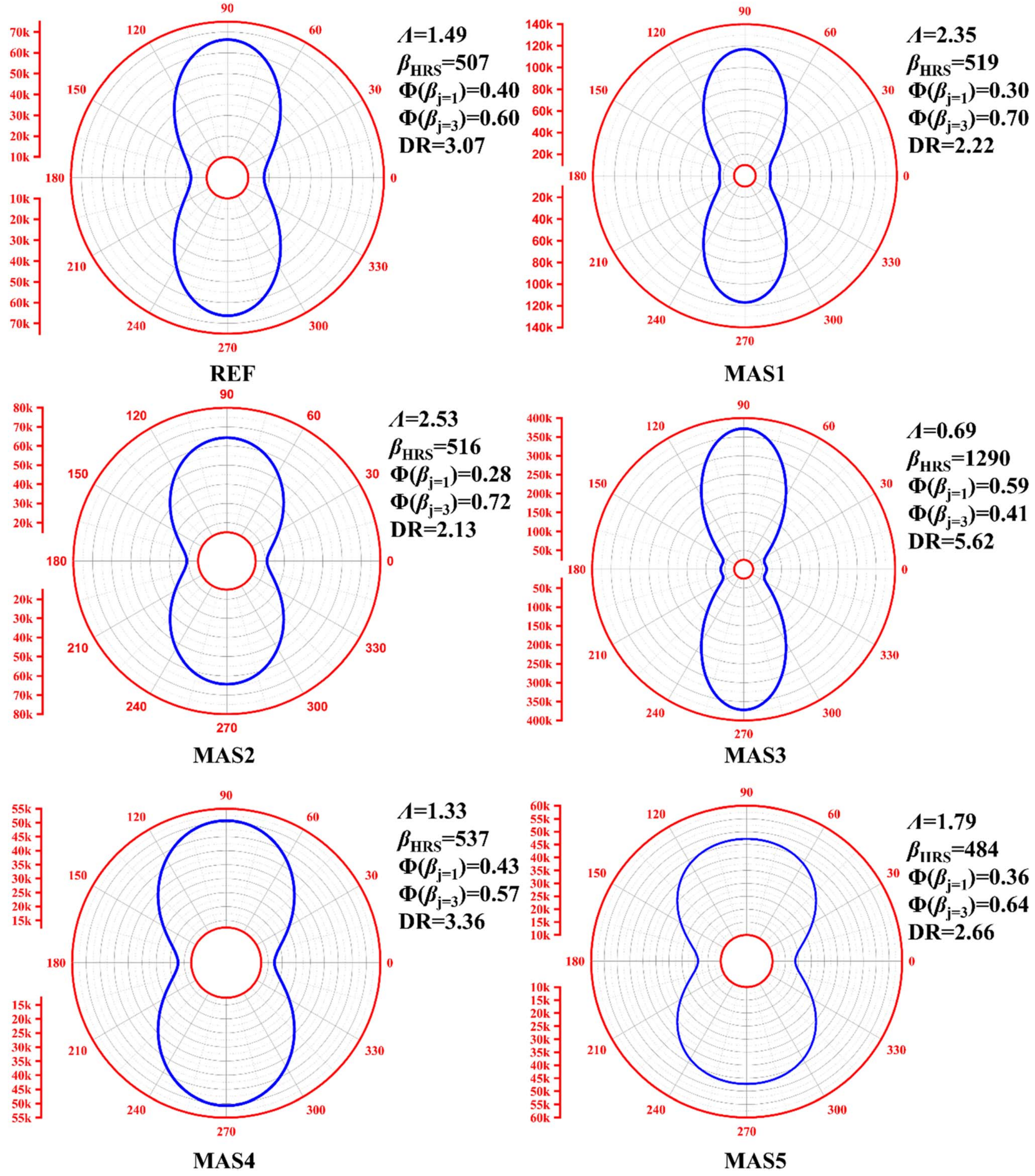

Fig. 11 The polar representation of harmonic light intensities *versus* polarization angle ω at λ = infinite wavelength.

LOL for π-electrons (LOL-π) is a quantum chemical tool used to visualize electron delocalization in conjugated systems. Fig. 13 shows three-dimensional isosurfaces representing the parts of the molecules where electrons are spread over multiple MOs. These regions highlight the areas that allow smooth electron mobility between atoms.[37,69,70]

A lower LOL-π value indicates greater π-electron delocalization, which enhances charge transfer and strengthens the NLO response. Moreover, the LOL-π isosurface is highly concentrated on C–C bonds, further confirming the role of π-electron delocalization in determining the NLO response of these compounds. As MAS3, with an NLO value of 3216.92 a.u.,

Table 12 Frequency-dependent $\gamma(-\omega;\omega,0,0)$ NLO properties of REF and MAS1–MAS5 for dynamic response under varying laser frequencies

Compounds	∞	1907 nm	1460 nm
REF	79 993.87	63 772.28	65 153.43
MAS1	104 653.00	84 237.08	85 797.83
MAS2	90 586.32	73 370.30	74 781.20
MAS3	144 893.30	118 973.50	122 086.10
MAS4	92 263.32	73 826.37	75 336.31
MAS5	96 416.62	78 454.03	80 065.55

Table 13 Investigation of frequency-dependent third-order NLO response $\gamma(-2\omega;\omega,\omega,0)$ of REF and MAS1–MAS5 compounds under optical frequency variation

Compounds	∞	1907 nm	1460 nm
REF	79 993.87	59 753.06	64 045.64
MAS1	104 653.00	78 849.30	83 667.54
MAS2	90 586.32	68 937.02	73 300.78
MAS3	144 893.30	114 078.80	124 211.60
MAS4	92 263.32	69 133.60	73 841.38
MAS5	96 416.62	74 098.00	79 149.40

likely exhibits lower LOL-π value 0.51 due to its stronger electron delocalization, facilitating a more efficient charge transfer mechanism. Conversely, MAS2, with a lower NLO value of 730.49 a.u., is expected to have higher LOL-π value 0.55, indicating relatively less π-electron delocalization. Thus, MAS3 is the best among these compounds in terms of NLO performance.

3.14 Radiative lifetime (τ_r)

The time required for an excited molecule to emit an electron is known as its radiative lifetime.[71] In optical devices, extending the radiative lifetime improves the chances of photon emission before energy dissipation through non-radiative pathways and strongly influences charge transfer efficiency.[72] Using eqn (22), the radiative lifetime is determined, with f_o (a.u.) as the first singlet excited-state value and E (cm^{-1}) as the excitation energy. All compounds were optimized at the singlet-excited state before calculations. MAS3 displays the highest radiative lifetime among the studied molecules. The synthesized compound MAS3 exhibit longer radiative lifetimes compared to REF, indicating higher charge transfer efficiency, which is essential for the performance of optoelectronic devices.

The extended radiative lifetimes might be caused by donor/acceptor substitution.[73] Excited-state retention in these compounds, facilitated by donor groups, enhances photon emission probability before energy dissipation. The longer radiative lifetimes, particularly for MAS3 and MAS1, indicate highly stable excited states and a prolonged period of charge separation. Such features are beneficial for applications including solar cells. Table 14 displays the measured light-harvesting efficiencies and radiative lifetimes. In conclusion, compared with MAS5, the synthesized compounds exhibit improved charge transfer capabilities, suggesting significant potential for photovoltaic, optoelectronic, and photochemical technologies.

3.15 Light harvesting efficiency (LHE)

Light harvesting efficiency refers to how effectively a substance absorbs light and generates charge carriers. Any material intended for solar cells must meet this requirement.[74] The LHE value allows prediction of the capability of designed molecules to absorb photons and subsequently move electrons into the semiconductor conduction band. The LHE was computed by using the formula represented in eqn (23).

The parameter "f_0" refers to the molecule's oscillator strength, reflecting its efficiency in absorbing light. The LHE values of the compounds are summarized in Table 14. MAS2 shows the greatest LHE among the MAS series, reflecting its

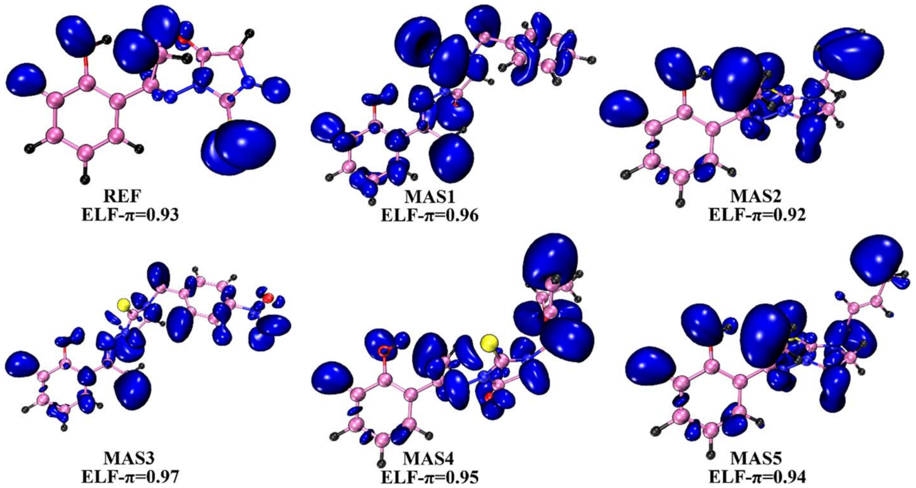

Fig. 12 The color-filled iso-surface maps of ELF-π of all the synthesized molecules REF and MAS1–MAS5 with their ELF-π values at B3LYP-D3 level of theory.

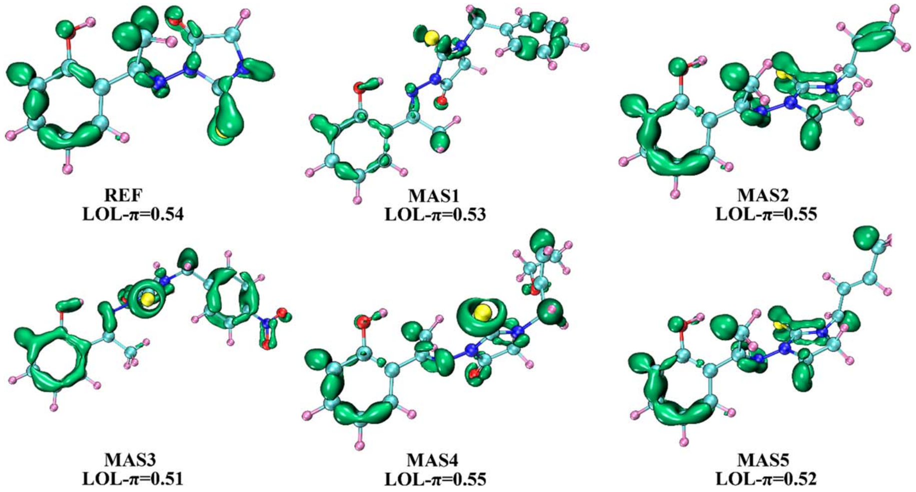

Fig. 13 The color-filled iso-surface maps of LOL-π of all the synthesized molecules REF and MAS1–MAS5 with their LOL-π values at B3LYP- D3 level of theory.

Table 14 The calculated value of LHE and radiative lifetime of all synthesized molecules REF and MAS1–MAS5 at D3-B3LYP level

Compounds	LHE	τ_r (ns)
REF	0.45	3.9
MAS1	0.32	5.7
MAS2	0.41	4.6
MAS3	0.34	8.8
MAS4	0.38	4.6
MAS5	0.37	4.8

enhanced ability to absorb light and generate charge carriers. The overall decreasing order is REF > MAS2 > MAS4 > MAS5 > MAS3 > MAS1. These molecules are highly effective in light absorption and charge carrier production, making them promising candidates for organic solar cells.

Fig. 14 provides a comparative analysis of two key photophysical properties – light harvesting efficiency (LHE) and radiative lifetime (τ_r) – for all compounds REF and MAS1–MAS5. The LHE values, depicted as sky-blue bars, reveal the compounds' ability to absorb light effectively. Notably, MAS2 stands out with the highest LHE value of approximately 0.388, indicating its superior light-absorbing capacity, whereas MAS3 exhibits the lowest value of around 0.34. In contrast, the radiative lifetime (τ_r) values, represented by the red line, signify the duration for which the compounds remain in the excited state before releasing energy as light. Interestingly, MAS3, despite its lower LHE value, displays the longest radiative lifetime of about 8.8 ns, suggesting potential applications in the fields like optoelectronics where prolonged excited-state behavior is beneficial. This understanding is vital for designing efficient light-harvesting or photonic materials that require both robust absorption and controlled excited-state lifetimes.

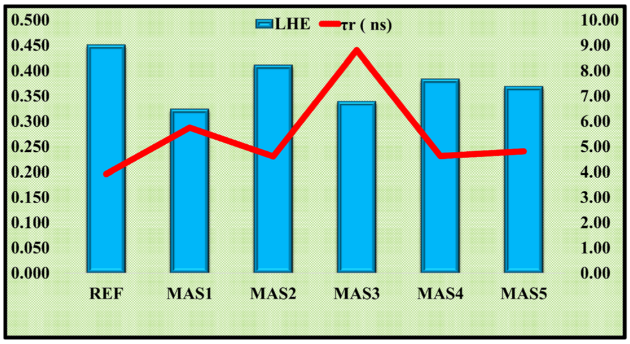

Fig. 14 Comparative analysis of light harvesting efficiency and radiative lifetime for all compounds REF and MAS1–MAS5.

While this study provides comprehensive insights into the NLO properties of *N*-alkylated thiohydantoin derivatives through combined experimental and computational approaches, certain limitations regarding theoretical models, though validated against experimental FTIR and ^{1}H and ^{13}C-NMR data, may not fully account for solvent–solute interactions, particularly in polar environments, which could influence electro-optical responses. Future research should explore the synthesis and characterization of additional derivatives with varied donor–acceptor motifs to expand the structure–property relationship library. Investigating solvent effects systematically, including explicit solvent modeling in simulations, would provide deeper insights into environmental influences on EFISHG and EOPE responses. Experimental validation of dynamic hyperpolarizabilities at multiple wavelengths and under external fields would bridge the gap between theoretical predictions and practical performance. Additionally, integrating these materials into device prototypes, such as electro-optic modulators or frequency doublers, could demonstrate their real-world applicability. Finally, exploring the role of aggregation effects, thin-film morphology, and interfacial interactions in solid-state devices would be critical for advancing these materials toward industrial applications in photonics and optoelectronics. This study lays a strong foundation for such endeavors, highlighting the potential of *N*-alkylated thiohydantoin derivatives as next-generation electro-optical materials.

4 Conclusion

This comprehensive study bridges experimental and computational approaches to elucidate the structure–property relationships of *N*-alkylated thiohydantoin derivatives, highlighting their potential for high-performance nonlinear optical devices. The integration of FTIR and NMR spectroscopy with DFT calculations confirmed the structural engineering of synthesized compounds, with the D3-B3LYP functional emerging as the most accurate for predicting vibrational and electronic properties. Among the studied compounds, the nitro-substituted MAS3 exhibits the narrowest HOMO–LUMO gap of 3.32 eV and the highest first hyperpolarizability ($\beta_{\text{tot}} = 3217$ a.u.), attributed to distinct ICT facilitated by its strong electron-withdrawing nitro group. This performance surpasses conventional references like *p*-NA and urea, underscoring the potential of thiohydantoin scaffolds in NLO applications. The MEP and FMO analyses provided visual evidence of charge separation and delocalization, while ELF and LOL studies quantitatively linked π-electron distribution to NLO efficacy. Frequency-dependent hyperpolarizability investigations revealed that γ values of MAS3 = 124 217 a.u. at 1460 nm are highly responsive to external fields, making it a candidate for electro-optic modulators and SHG devices. Thermodynamic assessments further validated the stability of these systems, with MAS3 showing optimal enthalpy (915.15 kJ mol^{-1}) and entropy (720.65 J mol^{-1} K^{-1}) for device integration. Practical applications demand thin-film fabrication and device testing to evaluate performance in real-world settings, such as optical switching or frequency conversion. Finally, this work establishes thiohydantoin derivatives, especially MAS3, as promising NLO materials, combining theoretical design principles with experimental validation. The insights gained here pave the way for tailored organic chromophores with applications in telecommunications, laser technologies, and quantum computing. Future research should focus on optimizing molecular architecture and exploring scalable fabrication techniques to transition these materials from the lab to industry. By addressing current limitations and expanding structural diversity, thiohydantoin-based systems could play a pivotal role in next-generation photonic technologies.

Conflicts of interest

The authors declare that they have no known competing financial interests or personal relationships that could have appeared to influence the work reported in this paper. The author also declares there is no conflict of interest.

Data availability

The data supporting this article have been included as part of the supplementary information (SI). Supplementary information: a brief description of any additional material omitted from the main body in the interest of presenting a clearer and more readable manuscript. See DOI: **https://doi.org/10.1039/d5ra06169e**.

Acknowledgements

The researchers would like to thank the Deanship of Scientific Research, Qassim University for funding the publication of this study.

References

1 P. Kaushik, *Innovative Physical Chemistry Perspectives*, Educohack Press, 2025.
2 X. Zhou, *et al.*, Surface and interfacial sciences for future technologies, *Natl. Sci. Rev.*, 2024, **11**(9), nwae272.
3 C. Kumar, *et al.*, Recent advancement in microwave photonics sensing technologies: A Review, *IEEE Sens. J.*, 2024, **24**(8), 11974–11985.
4 S. Aithal, P. Aithal and A. Bhat, Advancements in nonlinear optical materials: paving the way for future photonic devices, *Poornaprajna Int. J. Basic Appl. Sci.*, 2024, **1**(1), 1–58.
5 M. Hasnain, *et al.*, Dft Investigation of Functional Group Effects on the Structure of Tetraphenyl Porphyrin for Enhanced Nonlinear Optical Properties, *Chem. Pap.*, 2025, 1–16.
6 A. Ren, *et al.*, Emerging light-emitting diodes for next-generation data communications, *Nat. Electron.*, 2021, **4**(8), 559–572.
7 M. T. Hassan, Lightwave electronics: Attosecond optical switching, *ACS Photonics*, 2024, **11**(2), 334–338.
8 C. M. Schott, *et al.*, How to assess and predict electrical double layer properties. Implications for electrocatalysis, *Chem. Rev.*, 2024, **124**(22), 12391–12462.
9 R. Jana, *et al.*, Recent developments in the state-of-the-art optoelectronic synaptic devices based on 2D materials: a review, *J. Mater. Chem. C*, 2024, **12**(15), 5299–5338.
10 A. M. Arif, *et al.*, Spectroscopic behavior, FMO, NLO and substitution effect of 2-(1H-Benzo [d] imidazole-2-ylthio)-No-substituted-acetamides: Experimental and theoretical approach, *Dyes Pigm.*, 2019, **171**, 107742.
11 G. A. Nowsherwan, *et al.*, Advances in organic materials for next-generation optoelectronics: potential and challenges, *Organics*, 2024, **5**(4), 520–560.
12 H.-F. Wang, *et al.*, Quantitative spectral and orientational analysis in surface sum frequency generation vibrational spectroscopy (SFG-VS), *Int. Rev. Phys. Chem.*, 2005, **24**(2), 191–256.
13 G.-J. Cheng, *et al.*, Computational organic chemistry: bridging theory and experiment in establishing the mechanisms of chemical reactions, *J. Am. Chem. Soc.*, 2015, **137**(5), 1706–1725.
14 M. Akhtar, *et al.*, Tuning the NLO response of bis-cyclometalated iridium (III) complexes by modifying ligands: experimental and structural DFT analysis, *New J. Chem.*, 2021, **45**(12), 5491–5496.

15 P. K. Samanta and R. Misra, Intramolecular charge transfer for optical applications, *J. Appl. Phys.*, 2023, **133**(2), 020901.

16 Z.-y. Wang, *et al.*, Density functional theory studies on properties of cluster ConMoS (n= 1∼ 5): interatomic interactions, electronic properties, frontier orbitals, *J. Mol. Model.*, 2023, **29**(10), 326.

17 I. Shafiq, *et al.*, Exploration of promising key electronic and nonlinear optical properties of bifluorenylidene based chromophores: a TD-DFT/DFT approach, *Sci. Rep.*, 2025, **15**(1), 10701.

18 L. Xinju, X. Lan, and C. Huamin, *Laser Technology*, CRC press, Florida, 2010.

19 J. Liu, *et al.*, Recent advances in polymer electro-optic modulators, *RSC Adv.*, 2015, **5**(21), 15784–15794.

20 X. Xiao, *et al.*, Long-Lived Charge-Separated State in Naphthalimide–Phenothiazine Compact Electron Donor–Acceptor Dyads: Effect of Molecular Conformation Restriction and Solvent Polarity, *J. Phys. Chem. B*, 2023, **127**(31), 6982–6998.

21 T. Long, L. Zhang and Z. Cao, THF-Assisted CO2 Reduction Catalyzed by Electride Mg2EP: Insight from DFT Calculations, *J. Phys. Chem. A*, 2024, **128**(27), 5344–5350.

22 M. Khalid, *et al.*, Theoretical designing of non-fullerene derived organic heterocyclic compounds with enhanced nonlinear optical amplitude: a DFT based prediction, *Sci. Rep.*, 2022, **12**(1), 20220.

23 A. Hussain, *et al.*, Exploration of violet-to-blue thermally activated delayed fluorescence emitters based on "CH/N" and "H/CN" substitutions at diphenylsulphone acceptor. A DFT study, *Front. Chem.*, 2023, **11**, 1279355.

24 V. Trinquet, *et al.*, Second-harmonic generation tensors from high-throughput density-functional perturbation theory, *Sci. Data*, 2024, **11**(1), 757.

25 J. Liu, *et al.*, Mechanism exploration and catalyst design for hydrogen evolution reaction accelerated by density functional theory simulations, *ACS Sustain. Chem. Eng.*, 2023, **11**(2), 467–481.

26 W. Zhou and S.-P. Guo, Rational Design of Novel Promising Infrared Nonlinear Optical Materials: Structural Chemistry and Balanced Performances, *Acc. Chem. Res.*, 2024, **57**(4), 648–660.

27 B. Ali, *et al.*, Insight on the structural, electronic and optical properties of Zn, Ga-doped/dual-doped graphitic carbon nitride for visible-light applications, *J. Mol. Graphics Modell.*, 2023, **125**, 108603.

28 J. Deb, D. Paul and U. Sarkar, Density functional theory investigation of nonlinear optical properties of T-graphene quantum dots, *J. Phys. Chem. A*, 2020, **124**(7), 1312–1320.

29 A. Yousaf, A. M. Arif, N. Xu, J. Zhou, C. Y. Sun, X. L. Wang and Z. M. Su, A triazine-functionalized nanoporous metal–organic framework for the selective adsorption and chromatographic separation of transition metal ions and cationic dyes and white-light emission by Ln 3+ ion encapsulation, *J. Mater. Chem. C*, 2019, **7**(29), 8861–8867.

30 M. Li, *et al.*, Accurate prediction of the properties of materials using the CAM-B3LYP density functional, *J. Comput. Chem.*, 2021, **42**(21), 1486–1497.

31 X. Hou, Y. Ren and F. Fu, A density functional theory study on the electronic and adsorption characteristics of cyclo M 9 N 9 (M= B and Al), *J. Mol. Model.*, 2020, **26**, 1–10.

32 M. E. Frisch, *et al.*, *Gaussian 16*, Gaussian, Inc. Wallingford, CT, 2016.

33 T. Lu and F. Chen, Multiwfn: A multifunctional wavefunction analyzer, *J. Comput. Chem.*, 2012, **33**(5), 580–592.

34 R. Dennington, T. A. Keith, and J. M. Millam, *GaussView*, version 6.0.16, Semichem Inc Shawnee Mission KS, 2016.

35 F. Ahsan, S. Sarfaraz and K. Ayub, Unveiling the role of superalkali dopants in augmented nonlinear optical response of C13H10F12 Janus molecule–A DFT study, *Mater. Sci. Semicond. Process.*, 2025, **185**, 108995.

36 M. Khalid, *et al.*, NLO potential exploration for D–π–A heterocyclic organic compounds by incorporation of various π-linkers and acceptor units, *Arabian J. Chem.*, 2021, **14**(8), 103295.

37 A. M. Arif, *et al.*, N-(O-methoxyphenyl) aza-15-crown-5-ether derivatives: highly efficient and wide range nonlinear optical response based cation recognition, *J. Mol. Liq.*, 2020, **301**, 112492.

38 A. M. Arif, A. Yousaf, R. L. Zhong, M. Akhtar, S. Muhammad, H. L. Xu and Z. M. Su, Metal ions doped into merocyanine form of coumarin derivatives: nonlinear optical molecular switches, *J. Mol. Model.*, 2019, **25**(8), 212.

39 M. Khalid, *et al.*, Influence of End-Capped Modifications in the Nonlinear Optical Amplitude of Nonfullerene-Based Chromophores with a D− π–A Architecture: A DFT/TDDFT Study, *ACS Omega*, 2022, **7**(27), 23532–23548.

40 S. Sarwar, *et al.*, Deciphering the role of alkali metals (Li, Na, K) doping for triggering nonlinear optical (NLO) properties of t-graphene quantum dots: Toward the development of giant NLO response materials, *ACS Omega*, 2022, **7**(28), 24396–24414.

41 K. Ayub, Are phosphide nano-cages better than nitride nano-cages? A kinetic, thermodynamic and non-linear optical properties study of alkali metal encapsulated X 12 Y 12 nano-cages, *J. Mater. Chem. C*, 2016, **4**(46), 10919–10934.

42 S. Iftikhar, S. Hussain, S. Murtaza, D. Ali, S. Yousuf, M. A. Ali, M. S. Refat, *et al.*). Synthetic route for O, S-coordinated organotin (IV) aldehydes: Spectroscopic, computational, XRD, and antibacterial studies, *Appl. Organomet. Chem.*, 2024, **38**(8), e7581.

43 D. Ali, M. A. Ali, A. Yousuf and H. L. Xu, From charge transfer to sustainability: A multifaceted DFT approach to ionic liquid design, *Flat Chem.*, 2025, 100899.

44 M. Asif, *et al.*, Quantum chemical study on sensing of NH3, NF3, NCl3 and NBr3 by using cyclic tetrapyrrole, *Comput. Theor. Chem.*, 2021, **1199**, 113221.

45 M. Guo, M. Ji and W. Cui, Theoretical investigation of HER/OER/ORR catalytic activity of single atom-decorated graphyne by DFT and comparative DOS analyses, *Appl. Surf. Sci.*, 2022, **592**, 153237.

46 G.-Q. Mao, *et al.*, DFT-1/2 and shell DFT-1/2 methods: electronic structure calculation for semiconductors at LDA complexity, *J. Phys.: Condens. Matter*, 2022, **34**(40), 403001.

47 A. Ullah, *et. al.*, Crafting Optical Wonders: The Interplay of Electron Push–Pull Dynamics and π-Conjugation in Non–Linear Optics, *Next Mater.*, 2025, **9**, 101239.

48 M. Ibrahim, *et al.*, Unlocking the potential of Indolo-Carbazole derivatives: First-Principles insights into charge injection and optical switching applications, *J. Phys. Chem. Solids*, 2025, 113021.

49 Y.-M. Chai, *et al.*, X-ray structures, spectroscopic, antimicrobial activity, ESP/HSA and TD/DFT calculations of Bi (III) complex containing imidazole ring, *J. Mol. Struct.*, 2022, **1256**, 132517.

50 A. Yousuf, *et. al.*, Spectroscopic studies and Non-Linear optical response through C/N replacement and modulation of electron Donor/Acceptor Units on naphthyridine derivatives, *Spectrochim. Acta, Part A*, 2025, **329**, 125582.

51 Y. Qiu, *et al.*, DFT, FMO, ESP, Molecular Docking and Molecular Dynamics Simulations of Bis-2-(2-Phenethyl) Chromone as a Potential PPAR Agonist, *Lett. Org. Chem.*, 2023, **20**(7), 678–687.

52 A. Yousaf, *et al.*, A triazine-functionalized nanoporous metal–organic framework for the selective adsorption and chromatographic separation of transition metal ions and cationic dyes and white-light emission by Ln 3+ ion encapsulation, *J. Mater. Chem. C*, 2019, **7**(29), 8861–8867.

53 R. Nazir, *et al.*, An effective strategy for tuning nonlinear optical response of N-atom functionalized corannulene by alkali metals doping: First theoretical insight, *Comput. Theor. Chem.*, 2021, **1205**, 113430.

54 L. Xu, *et al.*, Recent progress in efficient organic two-photon dyes for fluorescence imaging and photodynamic therapy, *J. Mater. Chem. C*, 2020, **8**(19), 6342–6349.

55 S. Muhammad, *et al.*, A computational study for optical and nonlinear optical properties of distinctive V-shaped cyclopenta dithiophene derivatives, *Opt. Quantum Electron.*, 2023, **55**(10), 895.

56 A. Ullah, M. A. Ali, S. A. Siddique, M. Ibrahim, H. L. Xu, A. Rauf, M. Arshad, *et al.*). Quantum Chemical Insights into Metal-Ion Enhanced NLO Response of a Fluorescent Probe for Advanced Sensing Application, *J. Fluoresc.*, 2025, 1–21.

57 S. Chen, *et al.*, Superatoms (Li 3 O and BeF 3) induce phenalenyl radical π-dimer: fascinating interlayer charge-transfer and large NLO responses, *Dalton Trans.*, 2014, **43**(33), 12657–12662.

58 F.-W. Gao, *et al.*, Two-electron/24-center (2e/24c) bonding in novel diradical π-dimers, *Phys. Chem. Chem. Phys.*, 2016, **18**(42), 29041–29044.

59 F. T. Khan, *et al.*, Extrusion of carbon with SON in heterocycles for enhanced static and dynamic hyperpolarizabilities and light harvesting efficiencies, *Chem. Phys.*, 2025, 112761.

60 M. Ibrahim, *et al.*, Exploring the role of H-migration in the aromaticity, spectroscopic, photovoltaic and optical properties of planar heterocyclic compounds: a DFT study, *Phys. Chem. Chem. Phys.*, 2025, **27**(24), 12871–12885.

61 M. Hasnain, S. Urrehman, A. Yousuf, M. A. Ali, T. Fatima, S. Bibi and F. Q. Bai, DFT investigation of functional group effects on the structure of tetraphenyl porphyrin for enhanced nonlinear optical properties, *Chem. Pap.*, 2025, 1–16.

62 M. A. Ali, K. A. Nazish, M. Z. Qureshi, M. Mojzych, M. Arshad and H. L. Xu, Solvent-derived enhancement of electro-optic Pockels effect and second harmonic generation in heterocyclic/donor-acceptor functionalized α, β-unsaturated carbonyl compounds, *J. Mol. Liq.*, 2025, 128464.

63 A. M. Arif, *et al.*, Metal ions doped into merocyanine form of coumarin derivatives: nonlinear optical molecular switches, *J. Mol. Model.*, 2019, **25**, 1–8.

64 E. Marcano, *et al.*, Theoretical investigation of the static (dynamic) polarizability and second hyperpolarizability of DAAD quadrupolar push–pull molecules. A comparison among HF (TD-HF), DFT (TD-B3LYP), and MP2 (TD-MP2) methods, *Comput. Theor. Chem.*, 2012, **985**, 72–79.

65 L. Xu, *et al.*, The design strategies and applications for organic multi-branched two-photon absorption chromophores with novel cores and branches: a recent review, *J. Mater. Chem. C*, 2021, **9**(5), 1520–1536.

66 L. Xu, *et al.*, Simultaneously enhancing aggregation-induced emission and boosting two-photon absorption of perylene diimides through regioisomerization, *J. Mater. Chem. C*, 2022, **10**(18), 7039–7048.

67 J. C. Santos, *et al.*, An aromaticity scale based on the topological analysis of the electron localization function including σ and π contributions, *J. Chem. Theory Comput.*, 2005, **1**(1), 83–86.

68 R. Sukanya, *et al.*, Spectroscopic and quantum chemical computation on molecular structure, AIM, ELF, RDG, NCI, and NLO activity of 4-VINYL benzoic acid: a DFT approach, *J. Mol. Struct.*, 2022, **1253**, 132273.

69 P. Manjusha, *et al.*, Spectroscopic elucidation (FT-IR, FT-Raman and UV-visible) with NBO, NLO, ELF, LOL, drug likeness and molecular docking analysis on 1-(2-ethylsulfonylethyl)-2-methyl-5-nitro-imidazole: an antiprotozoal agent, *Comput. Biol. Chem.*, 2020, **88**, 107330.

70 M. J. Pramila, *et al.*, Structural insights, spectral, fluorescence, Z-scan, CH… O/NH… O hydrogen bonding and AIM, RDG, ELF, LOL, FUKUI analysis, NLO activity of N-2 (Methoxy phenyl) acetamide, *J. Mol. Struct.*, 2023, **1272**, 134140.

71 M. Bixon and J. Jortner, Long radiative lifetimes of small molecules, *J. Chem. Phys.*, 1969, **50**(8), 3284–3290.

72 L. C. Andreani, F. Tassone and F. Bassani, Radiative lifetime of free excitons in quantum wells, *Solid State Commun.*, 1991, **77**(9), 641–645.

73 S. ONeil, P. Rosmus and H. J. Werner, The radiative lifetime of A 1Πu C2, *J. Chem. Phys.*, 1987, **87**(5), 2847–2853.

74 S. Bai, *et al.*, High-performance planar heterojunction perovskite solar cells: Preserving long charge carrier diffusion lengths and interfacial engineering, *Nano Res.*, 2014, 7, 1749–1758.